Journal of Materials Chemistry A

ROYAL SOCIETY OF CHEMISTRY

PAPER

View Article Online
View Journal | View Issue

Check for updates

Cite this: J. Mater. Chem. A, 2026, 14, 19294

Elucidating the stabilizing effect of copper substitution in high voltage P2-type layered oxides for sodium-ion batteries

Remy Lecordier, [ab] Jon Serrano-Sevillano, *[a] Amaia Saracibar, [c] Carlos Escudero, [d] Gaël Minart, [a] Naiara Etxebarria, [a] François Fauth, [d] Carlo Marini, [d] Alessandro Longo, [ef] Lorenzo Stievano, [ghi] Marcus Fehse [ai] and Damien Saurel *[a]

P2-type layered sodium transition-metal oxides are promising high-energy cathodes for sodium-ion batteries but suffer from structural degradation and irreversible redox reactions particularly in the high-voltage region, resulting in rapid capacity fade. This study investigates how Cu substitution affects the structural evolution, redox mechanisms, and electrochemical performance of P2-type $Na_{2/3}Mn_{2/3}Ni_{1/3-y}Cu_yO_2$ (y = 0, 1/6, 1/3) cathodes for sodium-ion batteries. Cu substitution not only raises the average voltage of the practically delivered capacity upon extended cycling, thereby increasing energy density, but also shifts the undesired high-voltage plateau, associated with irreversible Ni^{4+}/Ni^{3+} and/or oxygen redox, to potentials beyond the practical operating window. This enables the partially substituted $Na_{2/3}Mn_{2/3}Ni_{1/6}Cu_{1/6}O_2$ to deliver 94.8 mAh g^{-1} at an average voltage of 3.45 V (320 Wh kg^{-1}) with 92% capacity retention after 100 cycles in half cells. *Operando* synchrotron X-ray diffraction reveals that this enhanced stability arises from a distinct phase evolution: while $Na_{2/3}Mn_{2/3}Ni_{1/3}O_2$ develops a P2 to O2 transition together with a loss of crystallinity in the form of stacking faults, the partially Cu-substituted sample forms a more reversible OP4 structure above 4.0 V with less pronounced interlayer-spacing changes. *Operando* X-ray absorption reveals sequential Ni^{2+} and Cu^{2+} oxidation to Ni^{3+} and Cu^{3+}, respectively. Extended X-ray absorption fine structure (EXAFS) analysis, corroborated by density functional theory (DFT) calculations, shows that in $Na_{2/3}Mn_{2/3}Ni_{1/6}Cu_{1/6}O_2$ NiO_6 and CuO_6 octahedra undergo almost-simultaneous opposite Jahn–Teller-distortion trends. This phenomenon reduces the effective overall Jahn–Teller-related lattice strain during (de)sodiation, compared to $Na_{2/3}Mn_{2/3}Ni_{1/3}O_2$ and $Na_{2/3}Mn_{2/3}Cu_{1/3}O_2$. Full-cell tests *vs.* hard carbon demonstrate the practical relevance, with $Na_{2/3}Mn_{2/3}Ni_{1/6}Cu_{1/6}O_2$ retaining 80% of its initial energy after 310 cycles and 50% after 1130 cycles at 100 mA g^{-1}, establishing partial Cu substitution as an effective route to stabilize high-voltage P2-type layered oxides for durable sodium-ion batteries.

Received 30th January 2026
Accepted 28th March 2026

DOI: 10.1039/d6ta00930a

rsc.li/materials-a

[a]Center for Cooperative Research on Alternative Energies (CIC energiGUNE), Basque Research and Technology Alliance (BRTA), Parque Tecnológico de Álava, Albert Einstein 48, Vitoria-Gasteiz 01510, Spain. E-mail: dsaurel@cicenergigune.com; jserrano@cicenergigune.com

[b]Materials Science and Technology Department, Basque Country University, Bilbao, Bizkaia, Spain

[c]Physical Chemistry Department, Pharmacy Faculty, Basque Country University, Álava, Vitoria-Gasteiz, Spain

[d]CELLS-ALBA Synchrotron Light Source, Cerdanyola del Vallès 08290, Spain

[e]BM16-FAME Beamline, The European Synchrotron Research Facility, 71 Avenue des Martyrs, F-38000, Grenoble, France

[f]Istituto Studio dei Materiali Nanostrutturati-CNR, Consiglio Nazionale delle Ricerche, Palermo 90146, Italy

[g]Institut Charles Gerhardt Montpellier (ICGM), Univ. Montpellier, CNRS, Montpellier 34293, France

[h]Réseau sur le Stockage Electrochimique de l'Energie (RS2E), CNRS, Amiens 80039, France

[i]ALISTORE-ERI European Research Institute, CNRS, Amiens 80039, France

1. Introduction

Sodium-based batteries have recently emerged as promising candidates to mitigate supply and cost risks associated with Li-based technologies. Compared with Li, Na is two or three orders of magnitude more abundant, more evenly distributed and one order of magnitude cheaper to produce, making Na-ion cells an attractive complementary option for large-scale energy storage.[1] Among the diverse families of Na-ion cathode materials, layered oxides with general formula Na_xMO_2 (where M is a transition metal) have attracted the most attention, as they offer some of the highest practical capacities together with structural flexibility and tuneable electrochemical properties.[2,3] As a consequence, layered oxides have been adopted as cathodes in most commercial Na-ion cells, underlining their practical relevance.[4–7]

Sodium layered oxides are mainly classified as either P2- or O3-type structures according to the Delmas classification.[8] Both structures are composed of alternating layers of sodium ions and edge-sharing MO_6 octahedra, but they differ in the stacking arrangement of the oxygen layers and the coordination environment of sodium. In O3-type oxides, oxygen layers follow an ABCABC stacking, with sodium ions occupying octahedral sites, while in P2-type oxides, the stacking is ABBA and sodium occupies prismatic sites. O3-type layered oxides are typically synthesised with near-stoichiometric sodium content ($x \approx 1$). This enables them to achieve higher practical capacities than their P2 counterparts, which can only be obtained in a Na-deficient form ($x \approx 2/3$). For this reason, O3 polymorphs have historically attracted more attention and appear in some of the first commercial Na-ion cells.[9–11] Nevertheless, P2 polymorphs should not be overlooked, as their lower accessible capacity is partially compensated by a higher average operating voltage.[12,13] This trade-off is well illustrated by O3-$NaMn_{0.5}Ni_{0.5}O_2$ (O3-NMN), which delivers 186 mAh g^{-1} at $\approx$ 3.0 V (558 Wh kg^{-1}),[14] compared to 130 mAh g^{-1} at $\approx$ 3.4 V (442 Wh kg^{-1}) for P2-$Na_{2/3}Mn_{2/3}Ni_{1/3}O_2$ (P2-NMN).[15] In other words, although P2 reaches only ~70% of the gravimetric capacity of the O3 phase, its higher operating voltage allows it to retain around 80% of the energy density. In both compounds, the redox-inactive Mn^{4+} stabilizes the layered framework and allows Ni to reside initially as Ni^{2+}, thereby enabling the full $Ni^{2+} \rightarrow Ni^{3+} \rightarrow Ni^{4+}$ redox sequence. Layered oxide cathodes that exploit this Ni-based double redox sequence are among the best-performing members of this family.[16–18]

Unfortunately, P2-$Na_{2/3}Mn_{2/3}Ni_{1/3}O_2$ shows limited cycle life, retaining only 52% of its capacity after 100 cycles, due to rapid structural degradation associated with the P2-O2 transition near the end of charge, leading to steep volume changes and irreversible oxygen redox.[15,19–22] While compositional tuning of O3-type Mn–Ni layered oxides has already yielded several formulations with improved cycling stability,[23,24] an equally effective strategy to stabilise P2-$Na_{2/3}Mn_{2/3}Ni_{1/3}O_2$ at high voltage has yet to be established. To tackle this issue, various compositional-optimisation strategies in P2-$Na_{2/3}Mn_{2/3}Ni_{1/3}O_2$ and related compositions have explored substitutions of Mn and/or Ni by other transition metals.[15,25] For example, Fe substitution involves a coupled cation exchange, where one Ni^{2+} and one Mn^{4+} are replaced by two Fe^{3+} ions. This shifts the redox activity towards higher voltage due to the Fe^{4+}/Fe^{3+} couple. Unfortunately, iron tends to migrate into tetrahedral sites, which leads to voltage hysteresis and sluggish Na^+ kinetics, ultimately degrading electrochemical performance.[26] In contrast, Mg and Zn dopants can stabilize the structure by suppressing phase transitions, but their limited solubility allows only a few percent to be incorporated before impurity phases appear. Moreover, their redox inactivity further reduces the achievable specific capacity.[27–29]

In this context, Cu has gained attention because the Cu^{3+}/Cu^{2+} redox couple voltage lies at a slightly higher potential than that of Ni^{3+}/Ni^{2+}.[30] Besides, since Ni^{3+} and Cu^{2+} are both Jahn–Teller active, their substitution are expected to affect not only the redox potential but also distortions of local octahedral coordination along with long range lattice strain, particularly at high voltage. Early work by Xu *et al.*[31] demonstrated reversible Cu redox activity in P2-$Na_{0.68}Mn_{0.66}Cu_{0.34}O_2$ with low polarisation, delivering ~74.5 mAh g^{-1} between 2.5 and 4.4 V. Follow-up studies showed that replacing Mn with Cu increased the average voltage (~3.6 V) and improved rate performance, although the overall capacity remained modest.[32–35] Ni substitution by Cu in P2-$Na_{2/3}Mn_{2/3}Ni_{1/3-y}Cu_yO_2$ has shown that intermediate Cu content ($y \approx 0.15$–0.20) enhances cycling stability and reduces hysteresis without substantially reducing the capacity below 4.2 V.[36,37] This has been attributed to a modification of the phase transition sequence near the end of charge. Specifically, the P2-O2 transition found in the unsubstituted compound is replaced by a P2-OP4 phase transition. This OP4 phase features alternating O- and P-stacking, which minimizes volumetric changes and improves structural reversibility.[36–38] Recent studies have highlighted the importance of transition-metal–oxygen bonding and its influence on interlayer stability and phase transition pathways in P2-type layered oxides.[39,40]

Despite these advances, several key aspects of how Cu substitution modifies the redox behaviour and structural evolution of Ni-based P2-type layered oxides remain unresolved. In particular, it is not clear how Cu substitution modifies (i) the sequence and relative contributions of Ni and Cu redox processes, (ii) the competition between OP4 formation and O2-type stacking faults at high voltage, and (iii) the associated Jahn–Teller distortions and lattice strain that ultimately control capacity fading. To address these questions, the series P2-$Na_{2/3}Mn_{2/3}Ni_{1/3-y}Cu_yO_2$ ($y = 0$, 1/6, 1/3) was systematically investigated by combining electrochemical testing with *operando* synchrotron X-ray diffraction, *operando* X-ray absorption spectroscopy and density functional theory (DFT) calculations, with a particular focus on linking structural evolution to long-term cycling stability in both half-cell and full-cell configurations.

2. Experimental methods

2.1. Synthesis

P2-$Na_{2/3}Mn_{2/3}Ni_{1/3}O_2$ (P2MnNi), P2-$Na_{2/3}Mn_{2/3}Ni_{1/6}Cu_{1/6}O_2$ (P2MnNiCu) and P2-$Na_{2/3}Mn_{2/3}Cu_{1/3}O_2$ (P2MnCu) materials were synthesized *via* a sol–gel method, adapted from the procedure reported by Wang *et al.*[41] Stoichiometric amounts of manganese(II) acetate tetrahydrate (Sigma-Aldrich, 99%), nickel(II) acetate tetrahydrate (Sigma-Aldrich, 99.995%), copper(II) acetate monohydrate (Sigma-Aldrich, 98%), and sodium carbonate (Sigma-Aldrich, 99.5%) were dissolved in deionized water. To account for sodium loss during high-temperature treatment, a 20% molar excess of sodium carbonate was used. Then, citric acid (Sigma-Aldrich, 99%) was added as a chelating agent in a 1 : 1 molar ratio with the total metal cations. The solution was stirred and heated to 80 °C until gelation occurred. The resulting gel was dried in a muffle furnace at 200 °C overnight. The dried precursor was manually ground and subsequently ball-milled using a Pulverisette P7 planetary mill at 250 rpm for 4 hours, with a ball-to-powder mass ratio of 14 : 1.

The homogenized powder was then placed in an alumina crucible and calcined at 900 °C for 12 hours under air, at a heating rate of 3 °C min^{-1}. After cooling to 180 °C, the material was immediately transferred into an argon-filled glovebox (O_2 and H_2O levels < 0.1 ppm). The final powder was reground before use. An approximate total of 3 g of the material was obtained per batch.

2.2. Electrode casting, cell assembly and electrochemical characterization

The slurry preparation and cell assembly of the cathode materials (P2MnNi, P2MnNiCu and P2MnCu) were conducted entirely within an argon-filled glovebox (H_2O and O_2 concentrations <5 ppm). Polyvinylidene fluoride (PVDF, Solvay) and conductive carbon (super C65, Imerys) were dried under vacuum at 120 °C overnight before being transferred into the glovebox. Electrode slurries were prepared using a weight ratio of 80 : 10 : 10 (active material : C65 : PVDF), mixed with 1-methyl-2-pyrrolidinone (NMP) using a magnetic stirrer. The slurry was then cast onto aluminium foil using the doctor blade technique to target a mass loading of 2–3 mg cm^{-2}. The coated laminates were dried under vacuum at 80 °C overnight, punched into 12 mm diameter electrodes, and then pressed at 2 tons for 1 minute. For comparison, $NaNi_{1/3}Fe_{1/3}Mn_{1/3}O_2$ (NMF111, Gelon) cathode electrodes were prepared following the same procedure except the active material ratio, which was 90 : 5 : 5 for active material : C65 : PVDF. The hard carbon anodes (Kuranode™ type 1 hard carbon) were prepared following the same NMP-based slurry casting method as for the cathode, mixing the active material with conductive carbon (super C 45, Imerys) and the PVDF binder at a ratio of 95 : 2 : 3.

Electrochemical half-cell tests were performed using three-electrode Swagelok-type cells. Sodium metal chips (AOT) served as both the counter and reference electrodes, while glass fibre grade D (Whatman) was used as the separator. The electrolyte (E-lyte) consisted of 1 M $NaPF_6$ dissolved in a 1 : 1 volume ratio of ethylene carbonate (EC) and propylene carbonate (PC). Galvanostatic cycling was carried out at room temperature on a Bio-Logic VMP3 potentiostat, at a rate of C/10 (about 25 mA g^{-1}). Full cell studies were conducted using CR2032 coin cells, with the same separator and electrolyte as for the half cell study. The 12 mm positive and negative electrodes were prepared with an areal loading of *ca.* 0.7 mAh cm^{-2}. The anode loading was adjusted to obtain an N/P ratio of 1.05, based on reversible capacities obtained in the first cycle in half cells (see Fig. 2 for P2MnNiCu and Fig. S1 for the HC), oversizing the anode by 5%. Full-cell cycling was conducted by performing two initial formation cycles at 15 mA g^{-1}, where the extracted capacity was limited to 106.3 mAh g^{-1} on the cathode side to match exactly the irreversible capacity of hard carbon during the first charge (330 mAh g^{-1}) followed by extended cycling at 100 mA g^{-1}. All electrochemical measurements were obtained from independent cells under identical conditions. The reported cycling data correspond to the average values, and the variability between cells is indicated by shaded areas representing the standard deviation.

2.3. X-ray diffraction characterization

Lab scale X-ray diffraction (XRD) patterns were recorded using a Bruker D8 Discover diffractometer equipped with a monochromatic Cu $K\alpha_1$ source ($\lambda = 1.54056$ Å) and a LynxEye-XE 1D detector. The patterns were collected over a 2θ range of 10–80° with a step size of 0.02° at 1 second per step. An airtight sample holder, sealed with Kapton foil and with a zero-background monocrystalline silicon base, was used for all measurements. The XRD patterns were refined by the Rietveld method using the FullProf software suite.[42,43] XRD patterns for structures containing stacking faults were simulated using FAULTS software.[44,45]

2.4. *Operando* X-ray diffraction measurements

Operando synchrotron X-ray diffraction (SXRD) experiments were conducted on P2MnCu and P2MnNiCu at the BL04-MSPD beamline[46] of the ALBA synchrotron (Barcelona, Spain), using a carousel stage, capable of sequentially measuring up to 8-coin cells.[47] Coin cells with an 8 mm diameter glass window were used (KIT Campus Transfer). XRD patterns were recorded every 10 minutes during galvanostatic cycling. The *operando* data were obtained in two different experiments; therefore, different wavelengths were used ($\lambda = 0.8273$ Å and $\lambda = 0.4959$ Å for P2MnCu and P2MnNiCu, respectively). The *operando* XRD patterns were refined using the FullProfAPP program.[48] The cells were mounted using the same components described in Section 2.2. All electrochemical data were collected with a VSP-3e Bio-Logic potentiostat using EC-Lab software in constant current mode. Cells were cycled at a C/30 rate (8.3 mA g^{-1}) within a voltage window of 1.5–4.5 V *versus* Na^+/Na.

2.5. Combined *operando* X-ray diffraction and *operando* X-ray absorption spectroscopy measurements

Operando XRD coupled with X-ray absorption spectroscopy (XAS) experiments were conducted at the BL16-NOTOS beamline[49] (ALBA synchrotron, Barcelona, Spain) on P2MnNi and P2MnNiCu. A customized electrochemical cell developed at CIC energiGUNE was employed,[50] featuring a 2 mm aperture in the sodium-side current collector and a beryllium window integrated into the plunger to enable X-ray transmission during cycling. The electrochemical cells were prepared under similar conditions to those previously explained in Section 2.2, but with a Whatman glass fibre grade QMA separator to avoid contamination effects in the XAS data acquisition. All electrochemical data were collected with a VSP-3e Bio-Logic potentiostat using EC-Lab software in constant current mode. Cells were cycled at a C/30 rate (8.33 mA g^{-1}) within a voltage window of 1.5–4.5 V *versus* Na^+/Na. The absorption K-edges of Mn (6.5 keV), Ni (8.3 keV), and Cu (8.9 keV) were measured in transmission mode sequentially and on the fly, alternating with XRD patterns at $\lambda = 0.9533$ Å. The *operando* XRD patterns were refined using the FullProfAPP program.[48] The acquired XAS data were processed and analysed using Athena[51] and MATLAB. The extensive XAS datasets were analysed with a chemometric approach, employed to reliably extract key information on oxidation states and local coordination of the probed transition metals during cycling.[52]

2.6. Computational methods

Superstructures containing various sodium-vacancy arrangements were generated using the Cluster Expansion and Statistical Mechanics (CASM)[53] code in combination with Python Materials Genomics (Pymatgen)[54] for each sodium content in P2-$Na_xMn_{2/3}Ni_{1/3-y}Cu_yO_2$ ($x = 2/3$, 1/2, 1/3, 0). The supercells considered in these calculations consisted of eight formula units, allowing for a detailed investigation of sodium-vacancy interactions and their impact on the system's energetics. A large number of configurations were initially screened based on their Ewald energies, and the 20 lowest-energy sodium-vacancy orderings were selected for each different sodium concentration.[55] The distribution of transition metals (Mn, Ni, and Cu) was fixed in a periodic, ordered pattern representative of the target composition (see Fig. S2 in the SI). DFT[56,57] calculations were carried out using the Vienna *Ab initio* Simulation Package (VASP),[58] with the Strongly Constrained and Appropriately Normed (SCAN)[59] meta-Generalized Gradient Approximation (GGA) functional to assess the system's electronic structure and energetics. A plane-wave energy cutoff of 520 eV was used, ensuring accurate total energy calculations and good convergence. A Monkhorst–Pack k-point mesh of $4 \times 4 \times 4$ was used to sample the Brillouin zone, with a Gamma-centred shift to improve accuracy. The force convergence criterion for ionic relaxation was set to 0.03 eV $Å^{-1}$, ensuring well-converged structures. Symmetrical constraints were turned off to allow complete relaxation.

The phase stability was analysed through a convex hull, using energy references from P2-$Na_{2/3}Mn_{2/3}Ni_{1/3-y}Cu_yO_2$ and P2-$Na_0Mn_{2/3}Ni_{1/3-y}Cu_yO_2$ ($y = 0$, 1/6, 1/3). The formation energy (ΔE_f) of each composition was evaluated relative to these reference structures using the following equation:

$$\Delta E_f = E_{Na_xMn_{2/3}Ni_{1/3-y}Cu_yO_2} - xE^{P2}_{Na_{2/3}Mn_{2/3}Ni_{1/3-y}Cu_yO_2} - (1-x)E^{P2}_{Na_0Mn_{2/3}Ni_{1/3-y}Cu_yO_2}$$

where the first term represents the total energy of the structure at x sodium content, while the second and third terms represent the total energy of the end members. A formation energy (ΔE_f) less than or equal to zero indicates a thermodynamically stable composition, while a positive value suggests that the structure is metastable or unstable relative to decomposition into a mixture of the reference phases.

2.7. Electron microscopy

Scanning electron microscopy (SEM) images were acquired with a FEI QUANTA 200 FEG scanning electron microscope operated at a voltage of 30 kV, using a secondary electron Everhart–Thornley detector (ETD). The samples were prepared by depositing powder onto a carbon tape substrate affixed to an aluminium pin holder.

2.8. X-ray Raman scattering spectroscopy

Ex situ X-ray Raman scattering spectroscopy (XRS) data of P2-$Na_xMn_{2/3}Ni_{1/3}O_2$ at different sodiation states were acquired at the ID20 beamline at the ESRF. A dedicated sample holder was assembled inside an argon-filled glovebox to prevent air exposure. The holder design included an aluminium foil window, chosen over Kapton to minimize the background signal and improve spectral quality in the soft X-ray range. Prior to measurement, the sample environment was purged with nitrogen to eliminate residual air and moisture. Data were collected under the synchrotron's 4-bunch mode, which offers reduced beam intensity and minimizes sample damage, albeit with longer acquisition times-typically around 6 hours per spectrum. Fluorescence from Mn was observed and carefully accounted for in the data processing. All measurements were collected at room temperature. To access different momentum transfer (q) regimes, spectra were recorded at multiple detector angles. Lower q-values were prioritized to enhance dipole transitions and reduce non-resonant background, while higher q configurations were avoided due to increased contributions from non-dipole transitions. This allowed reliable extraction of the Ni-L, Mn-L, and O-K edge features with bulk sensitivity, enabling detailed analysis of oxidation state changes and electronic structure evolution.

3. Results and discussion

The crystal structure of the synthesised P2-$Na_{2/3}Mn_{2/3}Ni_{1/3-y}Cu_yO_2$ ($y = 0$, 1/6, 1/3) compositions was examined by powder XRD (Fig. 1a). All reflections can be indexed to the hexagonal $P6_3/mmc$ space group, confirming that all three compositions adopt the targeted P2-type layered structure. Minor additional reflections marked with asterisks correspond to CuO impurities in the Cu-containing samples, quantified as 0.7% (±0.1) for P2MnNiCu and 2.1% (±0.2) for P2MnCu according to the Rietveld refinements shown in Fig. S3 and Tables S1–S3. The evolution of the a and c lattice parameters (right inset of Fig. 1a) follows Vegard's law: the cell parameters vary linearly with the Cu content, indicating the successful incorporation of Cu into the P2 structure despite the small amounts of CuO impurity. SEM images (Fig. S4) show no significant differences in morphology or particle size between the three compositions. All samples consist of platelet-shaped primary particles with well-defined hexagonal facets, typically 1–3 μm in lateral dimension and around 0.25–0.5 μm in thickness. Additionally, superstructure peaks are observed at $Q = 1.91$ $Å^{-1}$ and $Q = 2.00$ $Å^{-1}$ (left inset of Fig. 1a), corresponding to the (hkl) indices $\left(\frac{1}{6}\frac{2}{3}0\right)_H$ and $\left(\frac{1}{6}\frac{2}{3}1\right)_H$, respectively. Note that the peak indexing is given in the hexagonal $P6_3/mmc$ setting to facilitate comparison between compositions. These weak superstructure reflections are consistent with sodium-vacancy ordering reported for related P2-type layered oxides[37,60] and are present in all three samples, irrespective of the Cu content. Their assignment and evolution will be discussed in more detail in the *operando* XRD section below.

Although the diffraction patterns of all three compositions can be indexed in the hexagonal $P6_3/mmc$ space group, a closer inspection of the diffraction patterns reveals subtle deviations from ideal hexagonal symmetry for P2MnNi and P2MnCu, most clearly in the $Q = 4.2$–4.5 $Å^{-1}$ range (see Fig. 1b for P2MnNi and

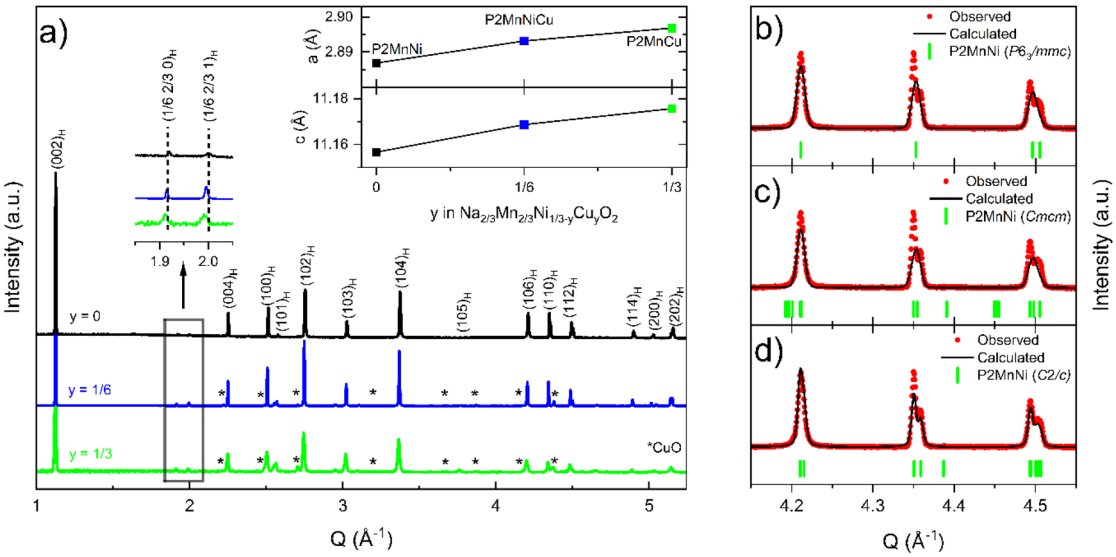

Fig. 1 (a) Powder XRD patterns of P2MnNi (black), P2MnNiCu (blue) and P2MnCu (green). The asterisks (*) show the main reflections of the CuO impurity peaks. The inset on the left is a zoom-in of the $Q = 1.8–2.1$ Å^{-1} range and on the right the evolution of the lattice parameters *vs.* the Cu content, deduced from Rietveld refinements. (b–d) Zoom-in of the Q range 4.15–4.55 Å^{-1} for the Rietveld refinements of P2MnNi using (b) $P6_3/mmc$, (c) $Cmcm$ and (d) $C2/c$ space groups. Red dots represent the observed XRD data, and black lines are the calculated diffraction patterns. The vertical green ticks mark the Bragg peak positions of the refined phase. The full refinement is provided in the SI (Fig. S5, Tables S1, S4 and S5).

full Rietveld refinements in Fig. S5). Such peak splitting indicates that the actual symmetry is lower than hexagonal. Although this material is commonly reported to crystallise in the hexagonal $P6_3/mmc$ space group, some authors have instead described related structures using larger hexagonal cells such as $P6_322$ or $P6_3$ to account for possible transition-metal ordering.[61] However, because Mn and Ni (or Mn and Cu) have very similar X-ray scattering factors, explicit in-plane superstructure ordering is challenging to evince reliably by XRD only. Additional studies have proposed that deviations from ideal hexagonal symmetry may arise from Mn–Ni cation ordering within the transition-metal layers, which can break the in-plane symmetry. The loss of the perfect hexagonal metric in the *ab* plane has been modelled as an orthorhombic distortion (often referred to as P′2 variants), using $C222_1$ [61] or $Cmcm$[34,62] space groups depending on whether explicit in-plane transition-metal ordering is considered or not, respectively. In our case, Rietveld refinements using the orthorhombic $Cmcm$ model improve the fit relative to $P6_3/mmc$, but the observed peak splitting is still not accurately reproduced (see Fig. 1c and Table S4).

An alternative explanation, inspired by lithium-rich layered oxides,[63] is that the symmetry lowering originates from a small distortion of the β-angle rather than a strong in-plane strain. The structures of P2MnNi and P2MnCu were therefore refined in the monoclinic $C2/c$ space group, following the approach reported by Dahn *et al.* (Fig. 1d).[64] The relation between the hexagonal and the monoclinic cells is shown in Fig. S6. The $C2/c$ space group gives the most accurate description of the diffraction pattern for both P2MnNi (Fig. S5 and Table S5) and P2MnCu (Fig. S7 and Table S6), as the monoclinic symmetry accommodates the small β-angle deviation responsible for the weak peak splitting. Importantly, this average model does not reproduce the weak Na-vacancy superstructure reflections at $Q \approx 1.91$ and 2.00 Å^{-1} (left inset of Fig. 1a), which require an explicit Na-ordering supercell description. Moreover, the fact that P2MnNi exhibits both Na-vacancy ordering and a monoclinic distortion, whereas P2MnNiCu exhibits even stronger Na-vacancy superstructure reflections yet retains hexagonal symmetry ($P6_3/mmc$ space group, see Fig. S3), indicates that Na ordering alone cannot explain the reduction in symmetry. Instead, the monoclinic distortion in the Ni-only phase likely reflects a significant contribution from Mn–Ni ordering within the transition-metal layers, an effect that is suppressed or strongly weakened in the Mn–Ni–Cu system. Interestingly, this peak splitting is absent in the intermediate P2MnNiCu composition, which is satisfactorily modelled using the hexagonal $P6_3/mmc$ unit cell. This apparent increase in symmetry is consistent with an enhanced intralayer transition-metal disorder, which seems to suppress the long-range transition metal ordering and cooperative Jahn–Teller distortions responsible for the monoclinic symmetry lowering in the end members.

The electrochemical performance of the different compositions is evaluated starting from the voltage-capacity curve of P2MnNi, shown in Fig. 2a, which exhibits the typical behaviour known for this compound.[65,66] Two pronounced plateaus of equal length are observed below 4.0 V, with a combined capacity of 83 mAh g^{-1}, which are attributed to the Ni^{3+}/Ni^{2+} redox couple reaction. The presence of two plateaus for a single redox reaction is attributed to different sodium-vacancy ordering rearrangements.[16,60] In the high voltage region above 4.0 V (coloured in orange), another pronounced plateau is observed, leading to a total capacity of 138.7 mAh g^{-1} at the end of charge. This plateau has been linked to the Ni^{4+}/Ni^{3+} redox couple and

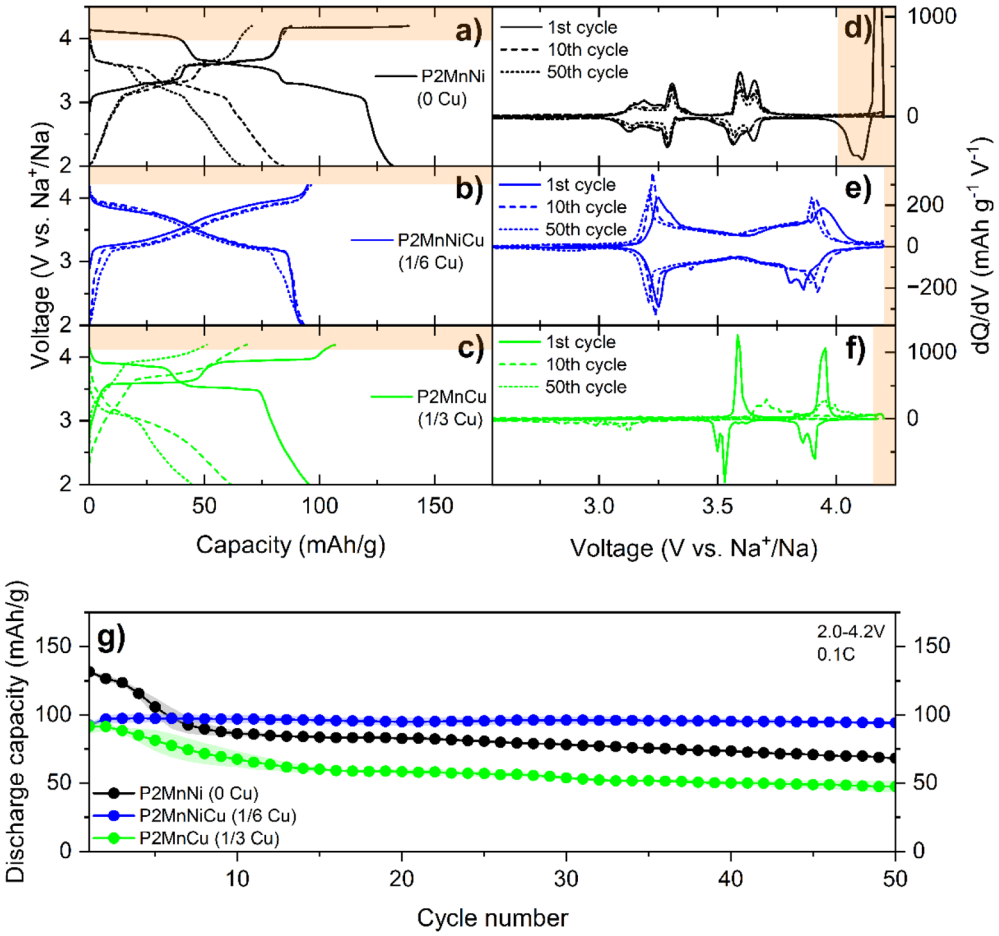

Fig. 2 (a–c) Voltage profiles of the P2-$Na_{2/3}Mn_{2/3}Ni_{1/3-y}Cu_yO_2$ materials ($y = 0$, 1/6, 1/3) and (d–f) their corresponding dQ/dV curves at the 1st, 10th and 50th cycles. (g) Capacity retention plot in half cells for each material for 50 cycles. The materials have been cycled at 0.1C in the 2.0–4.2 V voltage window. The cycling data represent the average values obtained from independent cells, with the shaded area indicating the standard deviation.

to oxygen redox, and it is known to be partially irreversible, leading to structural destabilization over prolonged cycling.[67]

The analysis of the mixed P2MnNiCu compound allows tracking how partial Cu substitution modifies the electrochemical response of P2MnNi. The voltage-capacity profile is much smoother than that for P2MnNi (see Fig. 2b) with an almost complete suppression of the voltage step that separates the two voltage plateaus in P2MnNi below 4 V. This is probably due to a decrease in cationic ordering induced by Cu substitution in the MO_2 layers. Cu substitution also has a strong effect above 4 V, where the voltage plateau observed in P2MnNi near 4.1 V disappears. This indicates that the high-voltage redox processes, likely involving $Ni^{4+/3+}$ and/or oxygen redox, are either suppressed or shifted to higher voltages beyond the operating window. Therefore, the overall initial capacity delivered below 4.2 V in P2MnNiCu is reduced (94.8 mAh g^{-1}) compared to the P2MnNi composition (138.7 mAh g^{-1}).

Finally, it should be noted that the voltage-capacity profile of the fully Cu substituted compound (Fig. 2c) resembles that of P2MnNi, also presenting a double plateau. This suggests that the transition-metal layer in P2MnCu may also exhibit intralayer transition metal ordering similar to P2MnNi. However, the high-voltage plateau that was observed in P2MnNi is not present in P2MnCu, as in the case of P2MnNiCu, resulting in significantly reduced charge capacity at 4.2 V (total capacity of 106.6 mAh g^{-1}). Notably, the average voltage of the first two plateaus during discharge is the highest in P2MnCu (3.60 V) compared to P2MnNiCu (3.45 V) and P2MnNi (3.36 V), indicating that Cu substitution gradually raises the cationic redox potential, as is clearly visible in the dQ/dV curves of Fig. 2d–f. Moreover, the substitution suppresses the redox activity at high potential (see orange areas in Fig. 2), impeding the oxidation of Cu^{3+} to Cu^{4+} and anionic oxygen redox participation. In short, Ni substitution by Cu raises the average voltage plateau observed below 4 V, suppresses the high voltage plateau and, in the case of partial substitution, smoothens the voltage plateau.

Fig. 2g (and Table S7) presents the cyclability of the three different compositions. The mixed P2MnNiCu exhibits markedly enhanced capacity retention, retaining 97% of its initial capacity after 50 cycles and still retaining 92% after 100 cycles (Fig. S8). Under the same conditions, P2MnNi retains only 52% of its initial capacity after 50 cycles and drops to 37% after 100

cycles (Fig. S8). Although P2MnNi initially delivers a higher capacity than P2MnNiCu, it rapidly declines within the first five cycles due to the disappearance of its high-voltage plateau. The fully Cu substituted P2MnCu performs even worse, since it reaches 41% of its initial capacity after 50 cycles. In this case, the rapid fading is accompanied by increasing voltage hysteresis, evidenced by the widening separation between charge and discharge peaks in the dQ/dV plots (Fig. 2f).

Expanding the voltage window to 4.5 V *vs.* Na^+/Na (Fig. 3) highlights further differences in electrochemical behaviour among the three compositions. P2MnNi delivers an initial charge capacity of 153.9 mAh g^{-1}, featuring a slightly extended high-voltage plateau, and the voltage jump near the end of charge indicates that the plateau is complete (orange area in Fig. 3a and d). Interestingly, the capacity fading appears less abrupt in the extended voltage window (Fig. 3g) compared to the previously discussed limited voltage window (Fig. 2f). The main loss of capacity with a cutoff voltage of 4.2 V arises from the proximity of the high voltage plateau to the cutoff voltage, making it very sensitive to any polarization build-up. As a result, when the voltage is limited to 4.2 V, this plateau only contributes to the first few cycles before being pushed outside of the defined voltage window by growing polarization. In contrast, increasing the cutoff voltage to 4.5 V allows the plateau to remain in the operating window for many more cycles as it accommodates the progressive polarization build up. Nevertheless, a gradual degradation is still observed at 4.5 V, and only about 64% of the initial capacity remains after 30 cycles. When the P2MnNiCu material is cycled to higher voltages, a new high-voltage plateau emerges at $\approx$ 4.28 V (Fig. 3b). By analogy with the P2MnNi compound, this plateau can be attributed to Ni^{3+} oxidation to Ni^{4+} and possibly to the onset of oxygen redox, yet at higher voltage than in the Ni-only compound (orange area in Fig. 3e), clearly underlining the Cu substitution effect of raising the operating voltage. Compared to P2MnNi, the high voltage plateau of P2MnNiCu is shorter due to the reduced nickel content, yielding a total charge capacity of 138.7 mAh g^{-1}. As with P2MnNi, this plateau also fades after only a few cycles. Finally, the fully Cu substituted P2MnCu material exhibits an even smaller high voltage plateau when cycled up to 4.5 V, giving a discharge capacity comparable to that obtained with a cutoff voltage of 4.2 V. Moreover, this plateau is absent in discharge, indicating poor reversibility of the underlying process (orange area in Fig. 3c and f).

This electrochemical experiment leads to two main conclusions. The first one is that, whenever a high-voltage plateau

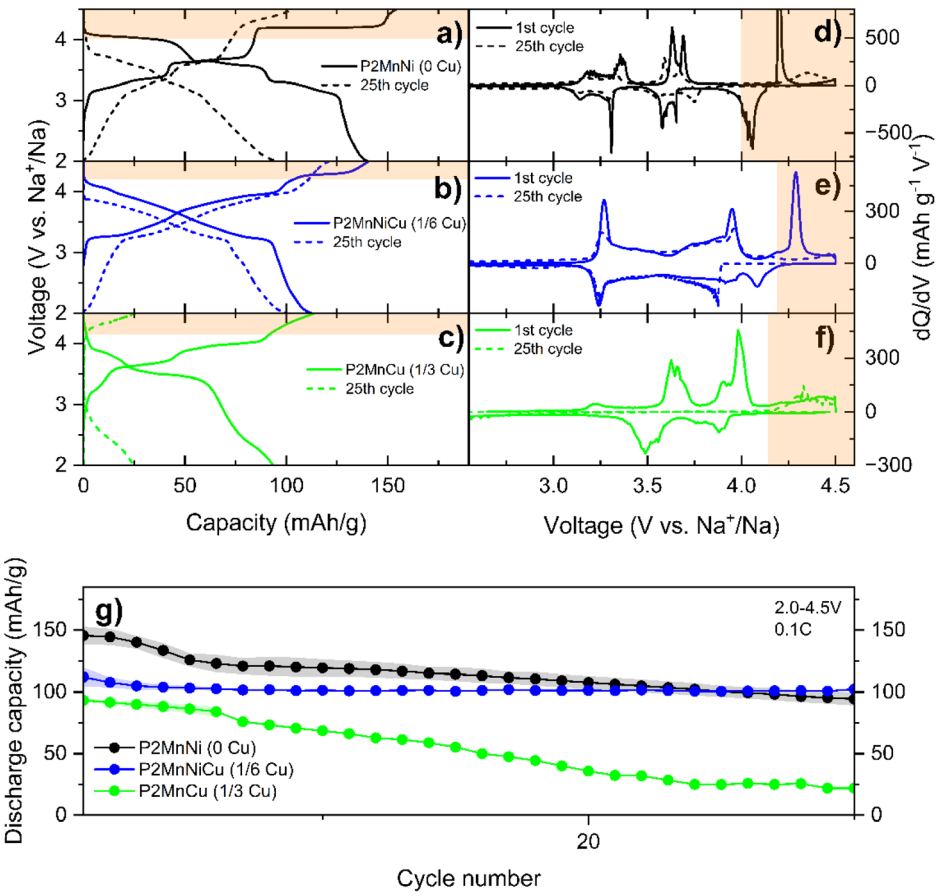

Fig. 3 (a–c) Voltage profiles of the P2-$Na_{2/3}Mn_{2/3}Ni_{1/3-y}Cu_yO_2$ materials (y = 0, 1/6, 1/3) and (d–f) their corresponding dQ/dV curves at the 1st and 25th cycles. The materials have been cycled at 0.1C in the 2.0–4.5 V voltage window. (g) Capacity retention plot in half cells for P2-$Na_{2/3}Mn_{2/3}Ni_{1/3-y}Cu_yO_2$ materials (y = 0, 1/6, 1/3) in the 2.0–4.5 V voltage window. The cycling data represent the average values obtained from independent cells, with the shaded area indicating the standard deviation.

associated with the Ni^{4+}/Ni^{3+} redox couple and/or oxygen redox is present, it tends to disappear upon cycling. Its underlying process can therefore be considered as a major source of capacity fading. The second observation is that partial substitution of Ni by Cu shifts this plateau to higher voltage and reduces its length, which improves the capacity retention in P2MnNiCu compared with P2MnNi at both 4.2 V and 4.5 V. For a fair comparison between the samples, P2MnNi was cycled to 4.0 V, hence excluding the high voltage plateau (see Fig. S9). Interestingly, P2MnNiCu still shows better capacity retention and considerably improved energy density when cycled to 4.2 V (97%) than P2MnNi cycled at 4.0 V (92%) for the same number of cycles. Furthermore, P2MnCu has poor capacity retention at 4.2 V even though no high voltage plateau is present. Taken together, these two observations suggest that a second, low voltage, degradation mechanism is occurring in parallel. A possible explanation could be related to the Jahn–Teller activity of the two redox species Ni^{3+} (moderate) and Cu^{2+} (strong), which induces local structural distortion, lattice strain and thereby structural fatigue upon cycling, which will be further discussed in the following.

To rationalise the electrochemical trends described above, including the rise in average voltage with Cu substitution, the evolution of the plateau length, and the contrasting cycling stabilities, DFT calculations were performed on the three compositions. The formation energies of different Na-vacancy configurations at different sodium contents were used to construct convex hulls from $x = 2/3$ to 0 and the corresponding voltage-composition curves (Fig. 4a and b). These calculated voltage profiles reproduce the main experimental trends: increasing Cu content lowers the formation energies of intermediate Na compositions ($Na_{0.5}$ and $Na_{0.33}$), deepening the convex hull and raising the average redox potential. This indicates that the transition metal substitution modifies phase stability and voltage profiles in P2-type oxides, in line with previous studies.[68,69] The computed curves are in good agreement with the experimentally obtained voltage profiles, capturing both the M^{3+}/M^{2+} redox activity below 4.0 V for all three compositions and the higher-voltage Ni^{4+}/Ni^{3+} redox processes experimentally observed for the Ni-containing materials. For P2MnCu, the calculations predict an additional high-voltage step (corresponding to the Cu^{4+}/Cu^{3+} redox process) located slightly above 4.5 V, which is consistent with the absence of a well-defined plateau in the electrochemical window investigated.

Besides predicting the electrochemical voltage profile, DFT modelling was also used to infer local structural evolution at distinct sodium content. Fig. 4c plots the difference between the two longest transition metal–oxygen bonds and the four shortest ones, reflecting the degree of elongation of the octahedra due to the Jahn–Teller distortion.[70] The evolution of each individual bond length is plotted in Fig. S10. The MnO_6 octahedra remain essentially unchanged across the full Na-content range, with Mn–O distances consistently around 1.9 Å. This confirms that manganese is redox inactive, as it is already in the +4 oxidation state in the fully sodiated phase and does not undergo further oxidation upon Na^+ extraction. In contrast, the NiO_6 and CuO_6 octahedra show significant changes upon desodiation. In

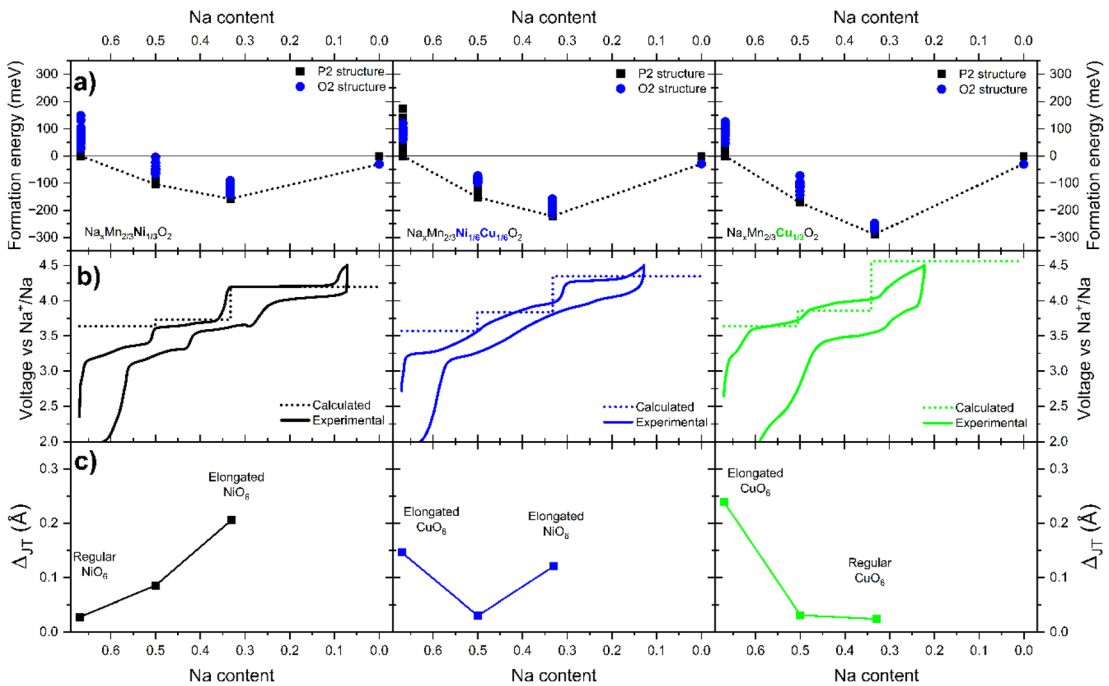

Fig. 4 (a) Calculated formation energies of P2 and O2 phases at different Na contents ($x = 0.67$, 0.5, 0.33 and 0) for each material plotted as a convex hull. (b) Experimental electrochemical curves (solid lines) compared to the calculated voltage profiles (dotted lines) for each material. (c) Evolution of the Jahn–Teller elongation amplitude difference (ΔJT) as a function of Na content, extracted from the fully relaxed most stable DFT structures for each material. ΔJT quantifies the difference between long and short TM–O bonds within each octahedron, highlighting the onset or suppression of Jahn–Teller distortions across compositions.

the pristine P2MnNi phase, the NiO_6 octahedra are essentially regular (ΔJT ~0 from Fig. 4c), with all the Ni–O distances clustered between 2.0 and 2.1 Å. Upon charging, ΔJT increases markedly, reflecting the onset of a Jahn–Teller distortion as Ni is oxidized to Ni^{3+}. This distortion originates from the characteristic splitting of the Ni–O bond lengths: four bonds contract to ~1.9 Å, while two remain elongated near 2.1 Å, as shown in Fig. S10a. The increase in ΔJT at lower Na content captures the growing amplitude of this octahedral distortion. The opposite behaviour is observed for CuO_6 octahedra. Since Cu^{2+} is Jahn–Teller active, the pristine structure exhibits distorted CuO_6 octahedra, which is reflected in Fig. 4c as a large ΔJT value at Na = 0.67. In this state, four Cu–O distances lie around 1.9–2.0 Å, while two bonds are elongated to 2.2–2.3 Å (Fig. S10c). Upon desodiation, these elongated bonds progressively shorten, and the six Cu–O distances converge toward 1.9–2.0 Å, leading to a marked decrease in ΔJT at lower Na content.

While the pure P2MnNi and P2MnCu structures individually undergo transitions between distorted and regular octahedra, the mixed P2MnNiCu compound distributes these structural strains more efficiently. The onset of NiO_6 distortion coincides with the reduction of distortion in CuO_6, keeping the overall number of distorted octahedra nearly constant. This fraction remains considerably lower (approx. 1/6 of all TM, Fig. 4c and S10b) than at the extreme points of the pure Cu (open-circuit voltage, OCV) and pure Ni (end of charge, EOC) analogues, where up to 1/3 of the transition metals sites are distorted. This balanced distortion-relaxation mechanism highlights a counterbalancing interplay between Ni and Cu environments, which likely contributes to the enhanced structural stability of the mixed-metal phase during cycling below the high-voltage plateau.

In order to analyse how the substitution of nickel by copper impacts the structural evolution of the materials during desodiation, *operando* SXRD experiments were carried out. Since the hexagonal and monoclinic phases share most of the peaks, and the hexagonal description is more commonly used in the literature, the *operando* SXRD peak evolution is described in the context of a hexagonal unit cell. Focus is first set on the structural evolution before the high voltage plateau, *i.e.*, until the voltage jump observed around 4.0 V in P2MnNi and 4.1 V in P2MnNiCu and P2MnCu, which corresponds to $x \approx 1/3$ (~80 mAh g^{-1}) according to Fig. 2. In this region, the SXRD patterns reveal a single-phase structural evolution for all three compounds (Fig. 5, full *Q* range in Fig. S11) with peak shifts and intensity changes that mirror reported behaviour of P2-type layered oxides. This agreement confirms that the structural response during Na extraction follows established trends in the literature.[66,71,72] The (002) reflection shifts to lower angles, while the $(100)_H$ and $(112)_H$ peaks shift to higher angles (Fig. S12), indicating an expansion along the *c*-axis due to reduced Na^+ screening of the O–O electrostatic repulsion and a contraction along the *ab* plane because of transition metal oxidation.[22,66]

P2MnNi and P2MnNiCu exhibit an overall comparable behaviour of constant peak shift, indicating a constant rate of change of the unit cell parameters, see Fig. 5a and b. However, at the voltage jump observed around 50 mAh g^{-1} (corresponding to $x \approx 0.5$) in P2MnNi, a small anomaly is observed in the evolution of the unit cell parameters. This is possibly related to Na-vacancy ordering. P2MnNiCu does not show a well-defined voltage jump near $x = 0.5$, nor any other discontinuity in its unit cell parameter evolution, probably a consequence of the lower transition metal ordering at the transition metal sites. P2MnCu, on the other hand, shows a very different behaviour. The $(002)_H$ peak is almost immobile until the first voltage jump corresponding to $x \approx 0.5$, where it quickly shifts to lower angles, inducing a pronounced jump in the evolution of the unit cell parameters, see Fig. 5c. A second plateau is observed from $x = 0.5$ to $x = 1/3$, corresponding to almost unvaried peaks and unit cell parameters, and a new jump is observed at the voltage jump observed near $x = 1/3$. The overall change of unit cell parameters is similar to the other two compounds, but the abrupt changes of unit cell parameters near $x = 0.5$ and $x = 1/3$ are likely to induce strain, thus contributing to the poor cyclability of P2MnCu. This is consistent with the overall volume contraction observed for all three compositions in Fig. 5. Part of these distinct structural changes can be related to the Jahn–Teller effect involving Ni^{3+} and Cu^{2+}. Among the three compounds, P2MnCu exhibits the most pronounced distortions, consistent with Cu^{2+} being the strongest Jahn–Teller ion and present already at OCV. P2MnNi displays anomalies in its unit cell parameters, near $x \approx 0.5$, when half of the Ni^{2+} ions are oxidized to Ni^{3+}, which exerts only a mild Jahn–Teller effect. In contrast, P2MnNiCu shows a much smoother evolution of lattice parameters, reflecting the reduced fraction of distorted TM sites in the partially substituted composition (around 1/6 of all transition metals, compared to up to 1/3 in the pure Ni or Cu analogues). This lower absolute number of simultaneously distorted environments contributes to the more gradual structural response observed during charge.

To track the evolution of the superstructure reflections identified in the pristine materials—namely the $\left(\frac{1}{6}\frac{2}{3}0\right)_H$ and $\left(\frac{1}{6}\frac{2}{3}1\right)_H$ peaks and their higher order analogues—and to get insight into the underlying ordering phenomena, the region of the diffraction patterns between the $(002)_H$ and the $(004)_H$ peaks (Fig. 6a) was monitored for P2MnNi and P2MnNiCu (and Fig. S13 for P2MnCu). At the beginning of charge ($x \approx 2/3$), all three compounds display this same pair of superstructure reflections, indexed as $\left(\frac{1}{6}\frac{2}{3}0\right)_H$ and $\left(\frac{1}{6}\frac{2}{3}1\right)_H$. As sodium is progressively extracted, these peaks disappear in all three materials, indicating that the corresponding ordered arrangement is destabilised upon desodiation, which supports their assignment to Na-vacancy ordering rather than static transition-metal ordering. Around 50 mAh g^{-1} ($Na_x \approx 0.5$) a new set of superstructure reflections, indexed as $\left(\frac{1}{4}\frac{1}{2}0\right)_H$ and $\left(\frac{1}{4}\frac{1}{2}1\right)_H$, appears in P2MnNi and P2MnNiCu. In P2MnCu, no clear superstructure reflections are observed at this Na content; instead, the high angle main Bragg peaks exhibit further shifts,

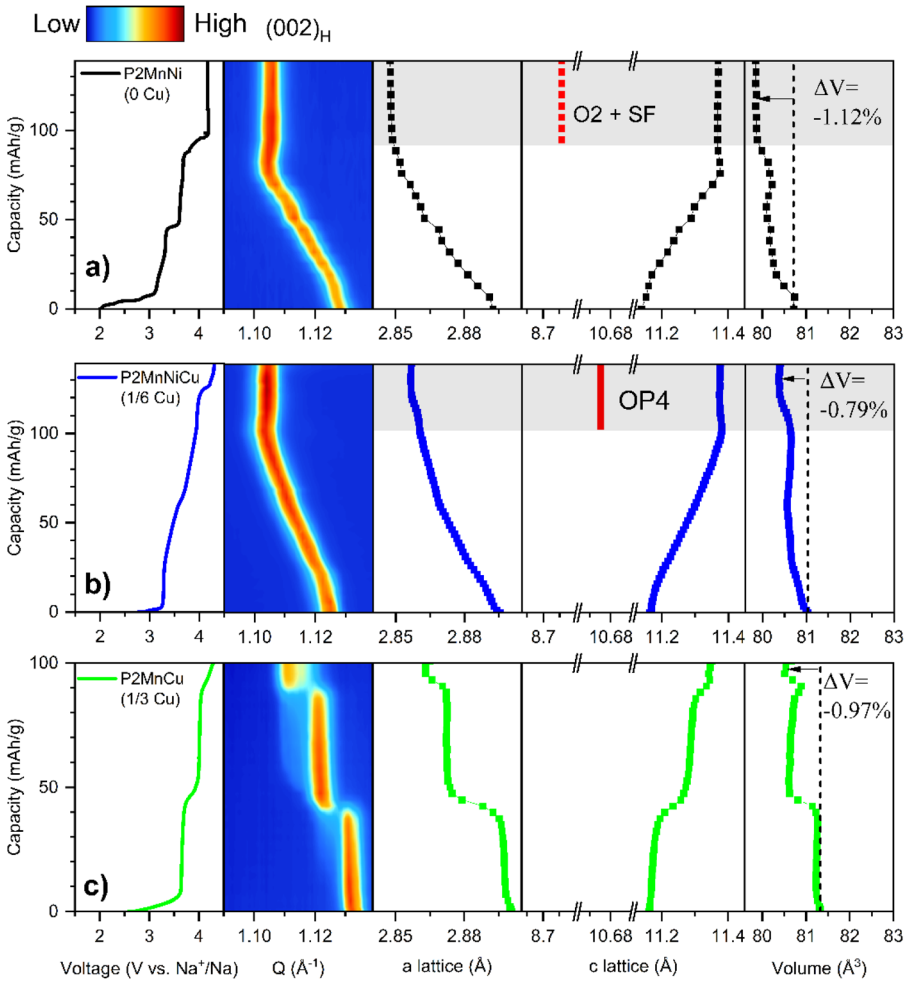

Fig. 5 Contour plots of *operando* SXRD during the first charge and their corresponding lattice parameter evolutions for (a) P2MnNi, (b) P2MnNiCu and (c) P2MnCu as a function of capacity. Grey shading indicates the high-voltage transition region. OP4 was treated as two interlayers, allowing direct comparison with the P2 parent. The complete *operando* SXRD contour plots over the full *Q*-range are provided in Fig. S11.

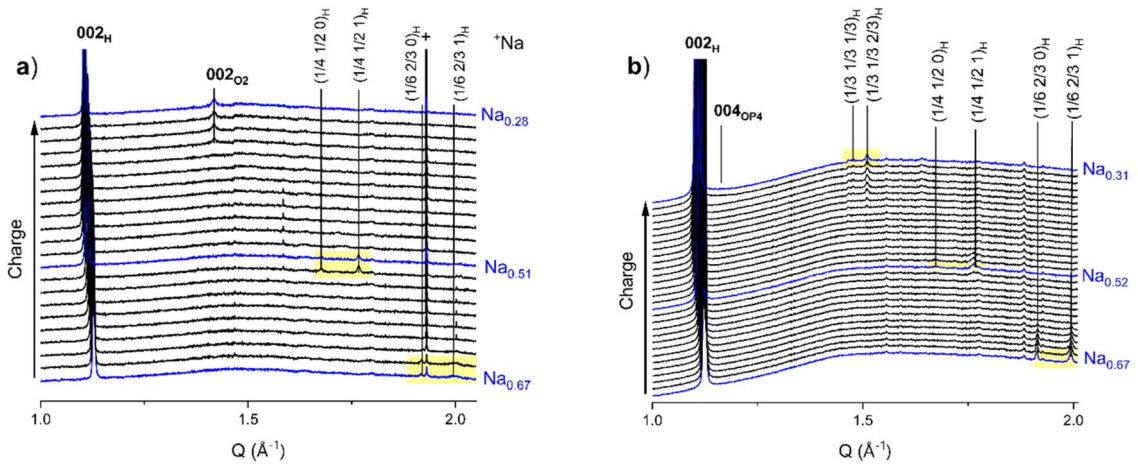

Fig. 6 *Operando* SXRD pattern evolution during the first charge for (a) P2MnNi and (b) P2MnNiCu.+markers indicate peak positions of Na metal arising from the cell stack.

splitting and shape changes, indicating a more complex structural response in this composition. This is probably related to the strong Jahn–Teller activity of Cu^{2+} ions. Finally, at higher degrees of desodiation (*i.e.*, $x \approx 1/3$), another ordering pattern appears, with new superstructural peaks indexed as $\left(\frac{1}{3}\frac{1}{3}\frac{1}{3}\right)_H$ and $\left(\frac{1}{3}\frac{1}{3}\frac{2}{3}\right)_H$. These reflections are clearly visible for P2MnNiCu and to a lesser degree, for P2MnCu, while for P2MnNi they are undetectable. Altogether, the appearance of distinct commensurate superstructure reflections at specific Na contents, while the transition-metal sublattice remains structurally intact (though progressively oxidizing), is characteristic of Na-vacancy ordering in P2-type layered oxides.[16,73] The salient differences between the three compositions—especially the suppressed $\left(\frac{1}{4}\frac{1}{2}l\right)_H$ ordering and the more complex evolution of the main Bragg reflections in P2MnCu—likely reflect the influence of their distinct local distortion patterns and Jahn–Teller activity, as suggested by the DFT analysis.

The study of the evolution of the SXRD patterns collected upon desodiation beyond the voltage jump that marks the onset of the high voltage plateau expected at $x \approx 1/3$ is presented in Fig. 7. P2MnNi undergoes an abrupt loss of crystallinity from $x = 0.33$ to $x = 0.28$, denoted by the $(10l)_H$ peak family (*i.e.*, $(102)_H$ or $(106)_H$) abruptly broadening while the $(h00)_H$, $(hk0)_H$, and $(00l)_H$ reflections remain unchanged. This asymmetric broadening is the typical signature of stacking faults, consisting of O interlayers randomly spreading into the P2 structure (see Fig. S14, Tables S8 and S9 for more details). This indicates that P2MnNi presents near $x \approx 1/3$ a second order transition from a well-defined P2 structure to a P2 structure containing a high density of O-type stacking faults. FAULTS simulations indicate that the fraction of stacking faults reaches approximately 10% (Fig. 7). Additionally, new weak reflections also appear at 1.41 and 4.64 $Å^{-1}$ (see Fig. 6 and S12), corresponding to the $(002)_{O2}$ and $(112)_{O2}$ peaks. These features indicate the apparition of O2-phase domains, suggesting a first-order transition from P2 to O2, in agreement with previous studies on similar layered oxide systems.[71,74,75] Both O-type stacking faults and the O2 phase are formed through gliding of the transition-metal-oxide layers, which coincides with an interlayer distance reduction (see lattice parameter *c* in Fig. 5a). These transitions can induce strains, potentially affecting the material's long-term structural stability upon cycling.[73,76] A possible explanation for the coexistence of O-type stacking faults and domains of the O2 phase is that the stacking faults are a way for the system to mitigate the strains that would be induced by the coexistence of well-developed P2 and O2 phases.

For P2MnNiCu, the $(10l)_H$ peak family of the P2 phase is also broadened after the voltage jump near $x \approx 1/3$, indicating the appearance of O-type stacking faults in the P2 phase similarly to P2MnNi, and new peaks are also observed indicating the nucleation of domains of a new long range ordered phase. However, in the case of P2MnNiCu, this new phase is the OP4 phase, as demonstrated by the FAULTS simulation in Fig. 7b. This OP4 structure alternates ordered stacking of prismatic (P-type) and octahedral (O-type) interlayers (see Fig. S14). While Yang *et al.*[36] and Wang *et al.*[41] reported no clear phase formation in this voltage range, our findings align with Kubota *et al.*'s work.[38] The emergence of the OP4 phase instead of an O2 phase helps explain the improved cyclability of this material at high voltage, as the coexistence of P and O layers mitigates the abrupt contraction of the interlayer distance typically associated with the P2 to O2 transition, accommodating structural strain during deep desodiation (see lattice parameter *c* in Fig. 5b).[38,71,77,78] It is possible that the formation of an OP4 phase instead of the O2 one observed for P2MnNi is related to the difference in Jahn–Teller activity evolution upon desodiation as well as the lower transition metal ordering due to the presence of three transition metals in P2MnNiCu.

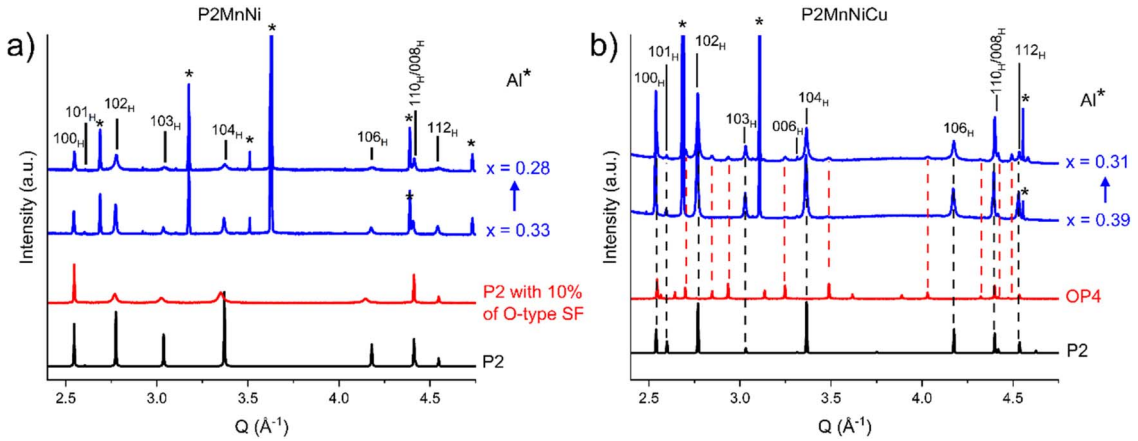

Fig. 7 Comparison between simulated XRD patterns (with FAULTS) and selected SRXD patterns for (a) P2MnNi and (b) P2MnNiCu materials. In panel (a), the red and black curves correspond to simulations of a P2 phase with 10% and 0% stacking faults, respectively, while the blue curves represent experimental SXRD patterns from *operando* data for compositions at $x = 0.33$ and $x = 0.28$. In panel (b), the red curve is the simulation of an ideal OP4 phase, and the black curve is the simulated ideal P2 phase. The blue curves are the experimental SXRD patterns of *operando* data for compositions at $x = 0.39$ and $x = 0.31$. Characteristic reflections (100_H, 101_H, 102_H, 103_H, 104_H, 006_H, 106_H, $110_H/008_H$, and 112_H) highlight the influence of stacking faults and phase transitions on structural evolution.

During discharge (resodiation), superstructure peaks reappear for both P2MnNi and P2MnNiCu at $x \approx 0.5$, consistent with the behaviour observed during charge and confirming the reversibility of Na-vacancy ordering in these compounds (see Fig. S15). At the end of discharge, the SXRD patterns of P2MnNi and P2MnNiCu closely resemble their OCV states: the main Bragg reflections return to their original positions, peak shapes and intensities are recovered, and no residual splitting or broadening is observed (Fig. S16a and b). In contrast, P2MnCu shows no detectable superstructure reflections at $x \approx 0.5$ (as during charge), and its SXRD pattern at the end-of-discharge differs slightly from the OCV one (see Fig. S16c). These discontinuous changes, combined with abrupt lattice shifts near $x \approx 0.5$ and $x \approx 1/3$, as observed in Fig. 5, suggest residual strain and disorder, consistent with the poor cyclability of P2MnCu.

Building on the structural and electrochemical insights from *operando* SXRD, the analysis now turns to *operando* XAS, focusing first on the X-ray absorption near edge spectroscopy (XANES) region and subsequently on EXAFS. Together, XANES and EXAFS enable the simultaneous study of both redox and local structural evolution. Fig. 8 shows the average position of the Ni K-edge for P2MnNi, allowing direct comparison with the *operando* XANES data of P2MnNiCu and highlighting how each transition metal contributes to the electrochemical mechanism with and without copper. The full evolution of the Ni edge for P2MnNi is shown as a contour plot in Fig. S17a. The *operando* XAS reveals a continuous shift of the Ni K-edge to higher absorption energies throughout charge up to 4.0 V, reflecting the oxidation of Ni^{2+} to Ni^{3+} (Fig. 8a–c). This redox process accounts for the capacity delivered up to ~83 mAh g^{-1} (corresponding to the extraction of ~0.3 Na^+ per formula unit) and is consistent with previous reports.[20,21] In contrast, the Mn K-edge position remains essentially unchanged, confirming that Mn is redox inactive in this voltage range (Fig. S18), as reported in the literature.[18] *Ex situ* XRS measurements of OCV *vs.* EOC samples confirm these findings, where the Ni L-edge displays a clear shift to higher energies upon charge while the Mn L-edge position remains unchanged, reflecting the absence of Mn oxidation (Fig. S19a and b, respectively). Above ~4.0 V, the Ni K-

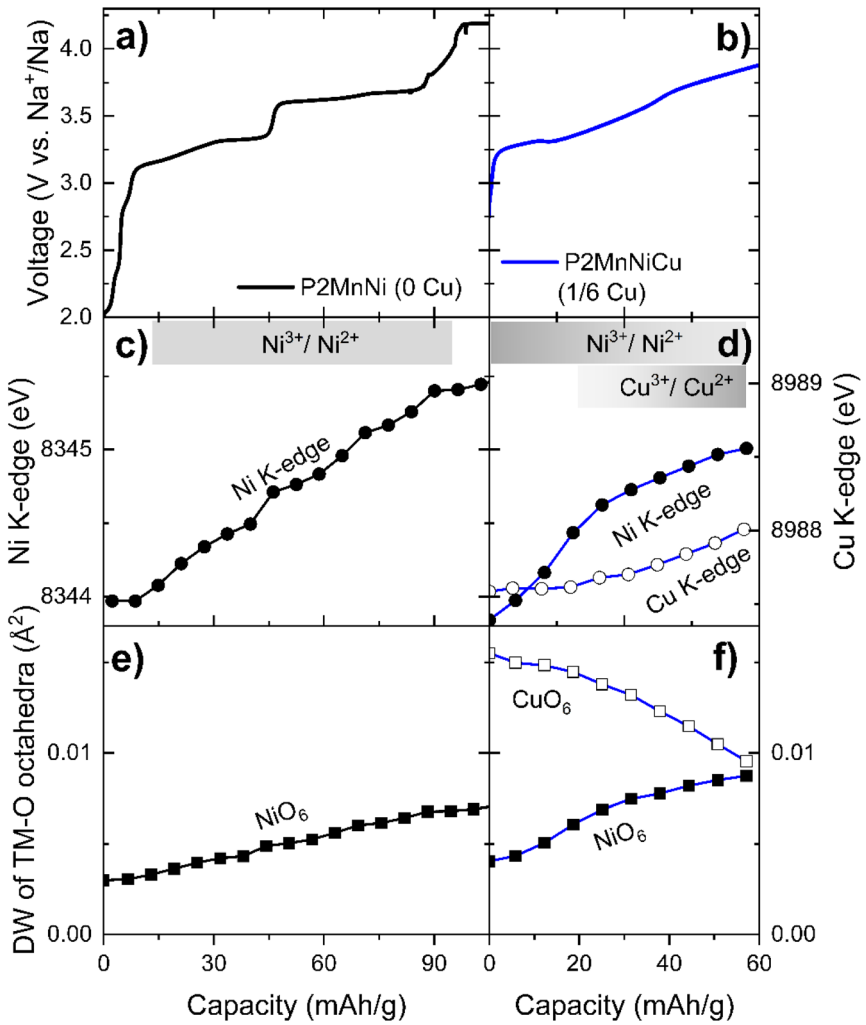

Fig. 8 *Operando* XAS Ni and Cu K-edge analysis of P2MnNi and P2MnNiCu during charge. (a and b) Voltage profiles *vs.* Na^+/Na, (c and d) their corresponding evolution of Ni and Cu K-edges and (e and f) the evolution of their Debye–Waller factors σ^2 for the Ni–O and Cu–O coordination shells, as a function of capacity.

edge shows minimal additional edge shift (Fig. 8c) indicating the waning of Ni redox activity, a behaviour aligned with the literature on similar compositions.[20]

In contrast, P2MnNiCu exhibits a sequential redox behaviour involving both Ni and Cu. Specifically, the Ni K-edge position in P2MnNiCu shows a steep shift within a narrower voltage window, with the most significant modification occurring at the early stages of sodium deintercalation. This sharper response is likely due to the reduced Ni content (1/6 *vs.* 1/3), resulting in an earlier fully oxidized state of Ni during the charge. As the Ni K-edge evolution slows down, the Cu K-edge begins to shift around 3.45 V, with a noticeable increase in the rate of change, suggesting that Cu becomes the dominant redox-active species at higher voltages (Fig. 8b–d). While the Cu K-edge shift is less pronounced than expected considering its contribution to capacity, this can be attributed to the strong Jahn–Teller distortion of the Cu^{2+} (3 d^9) centres, which modifies their ligand symmetry and ultimately the corresponding absorption edge position and shape.[34,79] Although this distortion introduces uncertainty in the precise determination of the Cu oxidation state by XANES, the redox activity of the Cu^{3+}/Cu^{2+} redox couple is salient. This sequential redox activity is at the origin of the distinct redox potentials of Ni and Cu, giving rise to two separate oxidation peaks in the electrochemical profiles. Therefore, these XAS results confirm the assignment of the dQ/dV peaks to the Ni^{3+}/Ni^{2+} and Cu^{3+}/Cu^{2+} redox couples at 3.25 and 3.94 V, respectively (Fig. 2e).

In addition to the oxidation state information obtained from XANES, *operando* EXAFS provides complementary insight into the evolution of the local transition-metal coordination environment during desodiation. The degree of distortion of the first-shell TM–O environment is quantified in Fig. 8e and f through the Debye–Waller factor (σ^2) extracted from EXAFS fitting. The underlying data are shown in the SI figures: contour plots of the EXAFS magnitude (Fig. S20) give a qualitative view of the evolution of the TM–O region during charge, while the fitted spectra and parameters (Fig. S21–S22 and Tables S10–S12) provide the quantitative basis for the σ^2 trends. Higher values correspond to increased local disorder, *i.e.*, more distorted octahedra, whereas lower values indicate more regular octahedra with equidistant bond distances.

In P2MnNi, the σ^2 value for Ni–O increases steadily with capacity (Fig. 8e), indicating growing local distortions as Ni^{3+} accumulates, consistent with the Jahn–Teller activity of the $3d^7$ configuration. In P2MnNiCu, the initial σ^2 value is larger than in P2MnNi due to the higher entropy induced by the presence of 3 different transition metals. Like for P2MnNi, the σ^2 for the Ni–O shell increases upon charge (Fig. 8f). In contrast, the σ^2 of the Cu–O shell decreases, and the CuO_6 octahedra become progressively more ordered as Cu participates in the redox reaction. This reciprocal evolution is visually observed in the EXAFS contour plots (Fig. S20), with a decrease in the Ni–O shell intensity and a concomitant increase in the Cu–O shell intensity with increasing capacity. This experimental trend mirrors the theoretical observations obtained by DFT, confirming that Cu participation alleviates/counterbalances the Ni^{3+}-driven Jahn–Teller distortion, supporting a strain-compensation mechanism that underpins the smoother structural response and improved cycling stability of P2MnNiCu.

Having demonstrated excellent cyclability of the P2MnNiCu cathode in half-cell tests across both moderate and high voltage windows (Fig. 2g and 3g), P2MnNiCu was evaluated in full-cell configuration. This allows the assessment of its energy density and long-term stability under a more realistic scenario. The inset of Fig. 9a displays the electrochemical cycling curve of the P2MnNiCu material in a full cell configuration with a hard carbon anode during the first 2 electrochemical cycles. The cell was cycled between 1.0 and 4.3 V at 100 mA g^{-1}, with two initial formation cycles at 15 mA g^{-1}. During the first cycle, the cathode delivered a reversible capacity of 92.9 mAh g^{-1} with an average discharge voltage of 3.48 V and an ICE of 86%. The charge–discharge profiles display smooth and reversible voltage curves with minimal polarization, suggesting efficient electrochemical kinetics. The initial energy of the studied material is 309 Wh kg^{-1} at 15 mA g^{-1} and 262 Wh kg^{-1} at 100 mA g^{-1}, of which 80% is retained after 310 cycles and nearly 50% is still retained after

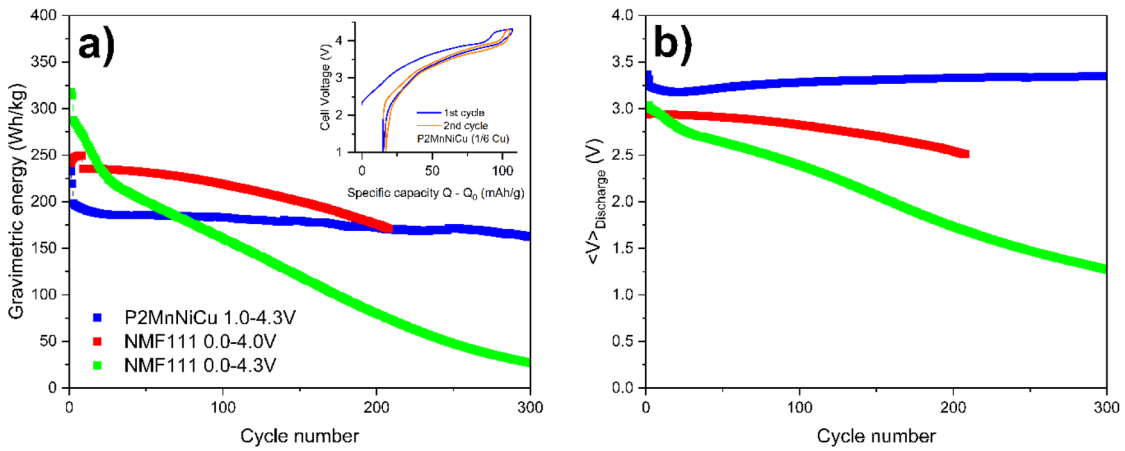

Fig. 9 (a) Comparison of long cycling performances of P2MnNiCu *vs.* NMF111 commercial materials in a full cell at 100 mA g^{-1}. The inset shows the formation cycles of the P2MnNiCu material in a full cell with a hard carbon anode cycled between 1.0 and 4.3 V at 15 mA g^{-1}. (b) Comparison of the average discharge voltage of P2MnNiCu *vs.* NMF111 commercial materials in a full cell.

1400 cycles (see Fig. S23). Fig. 9a shows the discharge energy evolution of the P2MnNiCu material over long-term cycling, compared to the commercial material O3-phase NMF111 cycled under two different voltage windows. At 100 mA g^{-1} and within a restricted voltage window (1.0–4.0 V) NMF111 retains 80% of the initial capacity at cycle 157. In contrast, when the operating voltage is comparable to the one used for P2MnNiCu (1.0–4.3 V), the NMF111 full cell shows a fast capacity decay. Consequently, the P2MnNiCu full cell energy density matches that of NMF111 near cycle 200, demonstrating an overall superior performance. Moreover, P2MnNiCu retains both energy and voltage more effectively (Fig. 9b). Note that there is a slight increase in the average discharge voltage upon cycling. The half-cell voltage profiles and dQ/dV curves remain essentially unchanged apart from a small polarization-induced decrease in the average discharge voltage (Fig. S24), meaning that this increase does not originate from the cathode. Instead, this effect arises from the hard-carbon anode. As the hard-carbon potential profile is composed of a sloping region and a low-potential plateau, the gradual upward shift in full-cell voltage is attributed to a progressive redistribution of Na storage toward the lower-potential plateau region during cycling. This lowers the anode potential *versus* Na^+/Na and, consequently, increases the measured full-cell discharge voltage. This highlights that the P2 phases, and especially those with partial Cu substitution, should not be overlooked as a serious contender for the O3 phases.

4. Conclusions

This work elucidates how partial Cu substitution in the P2-$Na_{2/3}Mn_{2/3}Ni_{1/3-y}Cu_yO_2$ series (y = 0, 1/6, 1/3) impacts both the redox and the structural mechanisms that ultimately control cyclability. The combined results of electrochemical testing, *operando* SXRD and XAS, as well as DFT calculations show that the Ni-rich end member (y = 0), which delivers the highest initial capacity, undergoes a high-voltage transformation encompassing a high density of O-type stacking faults and O2 phase nucleation, leading to strong lattice strains and rapid capacity fading. In contrast, the intermediate Cu content (y = 1/6) redirects the high-voltage pathway. While some stacking faults are still present, the dominant transformation at deep desodiation is the formation of a reversible OP4 phase, viewed as an alternating intergrowth of P- and O-type interlayers. This OP4 route diminishes the abrupt c-axis contraction and structural damage associated with the P2 to O2 transition and results in much improved capacity retention. XAS confirms sequential $Ni^{2+} \rightarrow Ni^{3+}$ and $Cu^{2+} \rightarrow Cu^{3+}$ oxidation, and the combination of DFT and EXAFS analysis of the TM–O bond distance reveals that in the mixed Ni/Cu composition the Jahn–Teller distortion of Ni^{3+} builds up as the initially strong distortion of Cu^{2+} is progressively relieved upon oxidation, keeping the overall population of distorted octahedra nearly constant. This counterbalancing supports a strain-compensation mechanism in which coupled Ni and Cu redox processes smooth the local structural response at high voltage. In contrast, the Cu-rich end member (y = 1/3) suffers from pronounced structural discontinuities near $x \approx 0.5$ and $x \approx 1/3$ despite a similar overall change in lattice parameters, likely driven by the strong Cu^{2+} Jahn–Teller effect and resulting in poor cycling stability. Using an intermediate Cu content (y = 1/6) gives a balance between accessible redox capacity and controlled high voltage stacking evolution. Tests in full cell configuration *vs.* hard carbon anodes show good stability, with ~80% of the initial capacity retained after 310 cycles at 100 mA g^{-1}. More broadly, these results highlight that carefully tuning the Ni/Cu ratio can balance the competing distortions and steer the P2 host toward a reversible OP4 pathway rather than a damaging P2 to O2 transition, providing a concrete design strategy for high-energy, long-life Na-ion cathodes.

Author contributions

Conceptualization: J. S., M. F. and J. S. S.; data curation: R. L., J. S. S., A. S., C. E., G. M., M. F., and A. L.; formal analysis: R. L., J. S. S., A. S., F. F., C. M., A. L., L. S., M. F., and D. S.; funding acquisition: F. F., L. S., and D. S.; investigation: R. L., J. S. S., A. S., F. F., C. M., A. L., L. S., M. F., and D. S.; supervision: J. S., A. S., M. F., L. S., and D. S.; validation: R. L., J. S. S., A. S., C. E., G. M., N. E., F. F., C. M., A. L., L. S., M. F., and D. S.; writing – original draft: R. L., J. S., M. F., and D. S.; writing – review & editing: R. L., J. S. S., A. S., C. E., G. M., N. E., F. F., C. M., A. L., L. S., M. F., and D. S. All authors have read and agreed to the published version of the manuscript.

Conflicts of interest

There are no conflicts to declare.

Data availability

Supplementary information (SI) is available. See DOI: https://doi.org/10.1039/d6ta00930a.

Acknowledgements

The authors are grateful for funding from grant PID2022-140823OB-I00 funded by MICIU/AEI/10.13039/501100011033 and ERDF, EU. JSS thankfully acknowledges the computer resources at Tirant and the technical support provided by the Universitat de València (UV) (QHS-2022-3-0006 and QHS-2023-2-0003). The authors are also grateful for access to ALBA synchrotron for beamtimes at the MSPD beamline through academic proposal 2022086967 and inhouse proposal 20250330050, as well as the NOTOS beamline through academic proposals 2023087724 and 2024028162. LS gratefully acknowledges financial support from the Agence Nationale de la Recherche (Labex STORE-EX and ANR-10-LABX-76-0).

References

1 R. Usiskin, Y. Lu, J. Popovic, M. Law, P. Balaya, Y. S. Hu and J. Maier, Fundamentals, Status and Promise of Sodium-Based Batteries, *Nat. Rev. Mater.*, 2021, **1**, 1020–1035, DOI: 10.1038/s41578-021-00324-w.

2 R. M. Gao, Z. J. Zheng, P. F. Wang, C. Y. Wang, H. Ye and F. F. Cao, Recent Advances and Prospects of Layered

Transition Metal Oxide Cathodes for Sodium-Ion Batteries, *Energy Storage Mater.*, 2020, **30**, 9–26, DOI: 10.1016/j.ensm.2020.04.040.

3 S. Mariyappan, Q. Wang and J. M. Tarascon, Will Sodium Layered Oxides Ever Be Competitive for Sodium Ion Battery Applications?, *J. Electrochem. Soc.*, 2018, **165**(16), A3714–A3722, DOI: 10.1149/2.0201816jes.

4 W. Zuo, A. Innocenti, M. Zarrabeitia, D. Bresser, Y. Yang and S. Passerini, Layered Oxide Cathodes for Sodium-Ion Batteries: Storage Mechanism, Electrochemistry, and Techno-Economics, *Acc. Chem. Res.*, 2023, **56**(3), 284–296, DOI: 10.1021/acs.accounts.2c00690.

5 L. Mu, S. Xu, Y. Li, Y. S. Hu, H. Li, L. Chen and X. Huang, Prototype Sodium-Ion Batteries Using an Air-Stable and Co/Ni-Free O3-Layered Metal Oxide Cathode, *Adv. Mater.*, 2015, **27**(43), 6928–6933, DOI: 10.1002/adma.201502449.

6 L. Zhao, T. Zhang, W. Li, T. Li, L. Zhang, X. Zhang and Z. Wang, Engineering of Sodium-Ion Batteries: Opportunities and Challenges, *Engineering*, 2023, 172–183, DOI: 10.1016/j.eng.2021.08.032.

7 S. Mariyappan, P. Desai, M. Morcrette and J.-M. Tarascon, From Lab to Market with Sustainable Sodium-Ion Batteries, *Nat. Sustain.*, 2025, **9**, 360–371, DOI: 10.1038/s41893-025-01701-x.

8 C. Delmas, C. Fouassier and P. Hagenmuller, Structural Classification and Properties of the Layered Oxides, *Physica B+C*, 1980, **99**(1), 81–85.

9 A. Bauer, J. Song, S. Vail, W. Pan, J. Barker and Y. Lu, The Scale-up and Commercialization of Nonaqueous Na-Ion Battery Technologies, *Adv. Energy Mater.*, 2018, **8**(17), 1702869, DOI: 10.1002/aenm.201702869.

10 A. Rudola, A. J. R. Rennie, R. Heap, S. S. Meysami, A. Lowbridge, F. Mazzali, R. Sayers, C. J. Wright and J. Barker, Commercialisation of High Energy Density Sodium-Ion Batteries: Faradion's Journey and Outlook, *J. Mater. Chem. A*, 2021, **7**, 8279–8302, DOI: 10.1039/d1ta00376c.

11 A. Rudola, R. Sayers, C. J. Wright and J. Barker, Opportunities for Moderate-Range Electric Vehicles Using Sustainable Sodium-Ion Batteries, *Nat. Energy*, 2023, **8**(3), 215–218, DOI: 10.1038/s41560-023-01215-w.

12 Y. Wang, R. Xiao, Y. S. Hu, M. Avdeev and L. Chen, P2-Na0.6[Cr0.6 Ti0.4]O2 Cation-Disordered Electrode for High-Rate Symmetric Rechargeable Sodium-Ion Batteries, *Nat. Commun.*, 2015, **6**, 7954, DOI: 10.1038/ncomms7954.

13 H. Yoshida, N. Yabuuchi, K. Kubota, I. Ikeuchi, A. Garsuch, M. Schulz-Dobrick and S. Komaba, P2-Type Na2/3Ni1/3Mn2/3−xTixO2 as a New Positive Electrode for Higher Energy Na-Ion Batteries, *Chem. Commun.*, 2014, **50**(28), 3677–3680, DOI: 10.1039/c3cc49856e.

14 Q. Huang, Y. Feng, L. Wang, S. Qi, P. He, X. Ji, C. Liang, S. Chen, L. Zhou and W. Wei, Structure Modulation Strategy for Suppressing High Voltage P3-O1 Phase Transition of O3-NaMn0.5Ni0.5O2 Layered Cathode, *Chem. Eng. J.*, 2022, **431**(4), 133454, DOI: 10.1016/j.cej.2021.133454.

15 W. Zhao, H. Kirie, A. Tanaka, M. Unno, S. Yamamoto and H. Noguchi, Synthesis of Metal Ion Substituted P2-Na2/3Ni1/3Mn2/3O2 Cathode Material with Enhanced Performance for Na Ion Batteries, *Mater. Lett.*, 2014, **135**, 131–134, DOI: 10.1016/j.matlet.2014.07.153.

16 D. H. Lee, J. Xu and Y. S. Meng, An Advanced Cathode for Na-Ion Batteries with High Rate and Excellent Structural Stability, *Phys. Chem. Chem. Phys.*, 2013, **15**(9), 3304–3312, DOI: 10.1039/c2cp44467d.

17 X. Wu, G. L. Xu, G. Zhong, Z. Gong, M. J. McDonald, S. Zheng, R. Fu, Z. Chen, K. Amine and Y. Yang, Insights into the Effects of Zinc Doping on Structural Phase Transition of P2-Type Sodium Nickel Manganese Oxide Cathodes for High-Energy Sodium Ion Batteries, *ACS Appl. Mater. Interfaces*, 2016, **8**(34), 22227–22237, DOI: 10.1021/acsami.6b06701.

18 J. Mao, X. Liu, J. Liu, H. Jiang, T. Zhang, G. Shao, G. Ai, W. Mao, Y. Feng, W. Yang, G. Liu and K. Dai, P2-Type Na2/3Ni1/3Mn2/3O2 Cathode Material with Excellent Rate and Cycling Performance for Sodium-Ion Batteries, *J. Electrochem. Soc.*, 2019, **166**(16), A3980–A3986, DOI: 10.1149/2.0211916jes.

19 T. Risthaus, D. Zhou, X. Cao, X. He, B. Qiu, J. Wang, L. Zhang, Z. Liu, E. Paillard, G. Schumacher, M. Winter and J. Li, A High-Capacity P2 Na2/3Ni1/3Mn2/3O2 Cathode Material for Sodium Ion Batteries with Oxygen Activity, *J. Power Sources*, 2018, **395**, 16–24, DOI: 10.1016/j.jpowsour.2018.05.026.

20 W. Zuo, F. Ren, Q. Li, X. Wu, F. Fang, X. Yu, H. Li and Y. Yang, Insights of the Anionic Redox in P2–Na0.67Ni0.33Mn0.67O2, *Nano Energy*, 2020, **78**, 105285, DOI: 10.1016/j.nanoen.2020.105285.

21 Y. Zhang, M. Wu, J. Ma, G. Wei, Y. Ling, R. Zhang and Y. Huang, Revisiting the Na2/3Ni1/3Mn2/3O2 Cathode: Oxygen Redox Chemistry and Oxygen Release Suppression, *ACS Cent. Sci.*, 2020, **6**(2), 232–240, DOI: 10.1021/acscentsci.9b01166.

22 H. Zhu, Z. Yao, H. Zhu, Y. Huang, J. Zhang, C. C. Li, K. M. Wiaderek, Y. Ren, C. J. Sun, H. Zhou, L. Fan, Y. Chen, H. Xia, L. Gu, S. Lan and Q. Liu, Unblocking Oxygen Charge Compensation for Stabilized High-Voltage Structure in P2-Type Sodium-Ion Cathode, *Advanced Science*, 2022, **9**(16), 2200498, DOI: 10.1002/advs.202200498.

23 J. Forero-Saboya, Y. Zhou, S. Browne, I. A. Moiseev, C. Pablos, J. Abou-Rjeily, A. Mboup, C. Alphen, L. Zhang, B. Li, A. M. Abakumov, J. M. Tarascon and S. Mariyappan, O3- vs P2-Type Nax(Ni,Zn,Mn,Ti)O2 Layered Oxides: Comparative Study on Electrode-Electrolyte Reactivity and Structural Stability for Cycling Performance, *Energy Storage Mater.*, 2025, **80**, 104423, DOI: 10.1016/j.ensm.2025.104423.

24 Q. Wang, S. Mariyappan, J. Vergnet, A. M. Abakumov, G. Rousse, F. Rabuel, M. Chakir and J. M. Tarascon, Reaching the Energy Density Limit of Layered O3-NaNi0.5Mn0.5O2 Electrodes via Dual Cu and Ti Substitution, *Adv. Energy Mater.*, 2019, **9**(36), 1901785, DOI: 10.1002/aenm.201901785.

25 Y. J. Guo, R. X. Jin, M. Fan, W. P. Wang, S. Xin, L. J. Wan and Y. G. Guo, Sodium Layered Oxide Cathodes: Properties,

Practicality and Prospects, *Chem. Soc. Rev.*, 2024, **4**, 7828–7874, DOI: 10.1039/d4cs00415a.

26 E. Talaie, V. Duffort, H. L. Smith, B. Fultz and L. F. Nazar, Structure of the High Voltage Phase of Layered P2-Na2/3-z [Mn1/2Fe1/2]O2 and the Positive Effect of Ni Substitution on Its Stability, *Energy Environ. Sci.*, 2015, **8**(8), 2512–2523, DOI: 10.1039/c5ee01365h.

27 Y. Li, K. A. Mazzio, N. Yaqoob, Y. Sun, A. I. Freytag, D. Wong, C. Schulz, V. Baran, A. S. J. Mendez, G. Schuck, M. Zając, P. Kaghazchi and P. Adelhelm, Competing Mechanisms Determine Oxygen Redox in Doped Ni–Mn Based Layered Oxides for Na-Ion Batteries, *Adv. Mater.*, 2024, **36**(18), 2309842, DOI: 10.1002/adma.202309842.

28 L. Xu, M. Song, J. Xie, M. Chen, W. Wu, Z. Tan, S. Qiu and X. Wu, Suppressing the P2–OP4 Phase Transition of Single-Crystal P2-Type Ni/Zn/Mn-Based Layered Oxide for Advanced Sodium-Ion Batteries, *Powder Technol.*, 2024, **448**, 120314, DOI: 10.1016/j.powtec.2024.120314.

29 Y. Zheng, J. Li, S. Ji, K. S. Hui, S. Wang, H. Xu, K. Wang, D. A. Dinh, C. Zha, Z. Shao and K. N. Hui, Zinc-Doping Strategy on P2-Type Mn-Based Layered Oxide Cathode for High-Performance Potassium-Ion Batteries, *Small*, 2023, **19**(39), 2302160, DOI: 10.1002/smll.202302160.

30 W. Zuo, J. Qiu, X. Liu, F. Ren, H. Liu, H. He, C. Luo, J. Li, G. F. Ortiz, H. Duan, J. Liu, M. S. Wang, Y. Li, R. Fu and Y. Yang, The Stability of P2-Layered Sodium Transition Metal Oxides in Ambient Atmospheres, *Nat. Commun.*, 2020, **11**(1), 3544, DOI: 10.1038/s41467-020-17290-6.

31 X. Shu-Yin, W. Xiao-Yan, L. Yun-Ming, H. Yong-Sheng, C. Li-Quan, S. Y. Xu, X. Y. Wu, Y. M. Li, Y. S. Hu and L. Q. Chen, Novel Copper Redox-Based Cathode Materials for Room-Temperature Sodium-Ion Batteries, *Chin. Phys. B*, 2014, **23**(11), 118202, DOI: 10.1088/1674-1056/23/11/118202.

32 W. Kang, Z. Zhang, P. K. Lee, T. W. Ng, W. Li, Y. Tang, W. Zhang, C. S. Lee and D. Y. Wai Yu, Copper Substituted P2-Type Na0.67CuxMn1-XO2: A Stable High-Power Sodium-Ion Battery Cathode, *J. Mater. Chem. A*, 2015, **3**(45), 22846–22852, DOI: 10.1039/c5ta06371j.

33 C. W. Mason, F. Lange, K. Saravanan, F. Lin and D. Nordlund, Beyond Divalent Copper: A Redox Couple for Sodium Ion Battery Cathode Materials, *ECS Electrochem. Lett.*, 2015, **4**(5), A41–A44, DOI: 10.1149/2.0041505eel.

34 E. J. Kim, T. Hosaka, K. Kubota, R. Tatara, S. Kumakura and S. Komaba, Effect of Cu Substitution in P′2- and P2-Type Sodium Manganese-Based Oxides, *ACS Appl. Energy Mater.*, 2022, **5**(10), 12999–13010, DOI: 10.1021/acsaem.2c02581.

35 D. Wang, F. Zou, W. Lin, X. Zhang, X. Zhang, X. Qi, S. Xu, H. Mao, D. Xiao, S. Lu, B. Guo, Y. S. Hu and Y. Lyu, Transition Metal Slab Gliding: One Key Process for Activating Anionic Redox Reaction in P2-Type Transition Metal Oxide Cathodes, *Advanced Science*, 2025, **12**(26), 2501852, DOI: 10.1002/advs.202501852.

36 L. Yang, S. h. Luo, Y. Wang, Y. Zhan, Q. Wang, Y. Zhang, X. Liu, W. Mu and F. Teng, Cu-Doped Layered P2-Type Na0.67Ni0.33-XCuxMn0.67O2 Cathode Electrode Material with Enhanced Electrochemical Performance for Sodium-Ion Batteries, *Chem. Eng. J.*, 2021, **404**, 126578, DOI: 10.1016/j.cej.2020.126578.

37 L. Zheng, J. Li and M. N. Obrovac, Crystal Structures and Electrochemical Performance of Air-Stable Na2/3Ni1/3-XCuxMn2/3O2 in Sodium Cells, *Chem. Mater.*, 2017, **29**(4), 1623–1631, DOI: 10.1021/acs.chemmater.6b04769.

38 K. Kubota, Y. Yoda and S. Komaba, Origin of Enhanced Capacity Retention of P2-Type Na2/3Ni1/3-XMn2/3CuxO2 for Na-Ion Batteries, *J. Electrochem. Soc.*, 2017, **164**(12), A2368–A2373, DOI: 10.1149/2.0311712jes.

39 X. Cai, Z. Shadike, N. Wang, X. L. Li, Y. Wang, Q. Zheng, Y. Zhang, W. Lin, L. Li, L. Chen, S. Shen, E. Hu, Y. N. Zhou and J. Zhang, Constraining Interlayer Slipping in P2-Type Layered Oxides with Oxygen Redox by Constructing Strong Covalent Bonds, *J. Am. Chem. Soc.*, 2025, **147**(7), 5860–5870, DOI: 10.1021/jacs.4c14587.

40 X. Cai and Z. Shadike, Phase Transition Regulation Mechanisms in P2-Type Oxide Cathodes, *Adv. Mater.*, 2026, **38**(14), e21162, DOI: 10.1002/adma.202521162.

41 L. Wang, Y. G. Sun, L. L. Hu, J. Y. Piao, J. Guo, A. Manthiram, J. Ma and A. M. Cao, Copper-Substituted Na0.67Ni0.3-XCuxMn0.7O2 Cathode Materials for Sodium-Ion Batteries with Suppressed P2-O2 Phase Transition, *J. Mater. Chem. A*, 2017, **5**(18), 8752–8761, DOI: 10.1039/c7ta00880e.

42 J. Rodriguez-Carvajal, Recent Advances in Magnetic Structure Determination Neutron Powder Diffraction, *Physica B*, 1993, **192**(93), 55–69.

43 J. Rodriguez-Carvajal, J. Gonzalez-Platas and N. A. Katcho, Magnetic Structure Determination and Refinement Using FullProf, *Acta Crystallogr., Sect. B:Struct. Sci., Cryst. Eng. Mater.*, 2025, **81**(Pt 3), 302–317, DOI: 10.1107/S2052520625003944.

44 M. Casas-Cabanas, M. Reynaud, J. Rikarte, P. Horbach and J. Rodríguez-Carvajal, FAULTS: A Program for Refinement of Structures with Extended Defects, *J. Appl. Crystallogr.*, 2016, **49**(6), 2259–2269, DOI: 10.1107/S1600576716014473.

45 M. Casas-Cabanas, J. Rodríguez-Carvajal and M. R. Palacín, FAULTS, a New Program for Refinement of Powder Diffraction Patterns from Layered Structures, *Z. Kristallogr.*, 2006, **23**(23), 243–248.

46 F. Fauth, R. Boer, F. Gil-Ortiz, C. Popescu, O. Vallcorba, I. Peral, D. Fullà, J. Benach and J. Juanhuix, The Crystallography Stations at the Alba Synchrotron, *Eur. Phys. J. Plus*, 2015, **130**(8), 160, DOI: 10.1140/epjp/i2015-15160-y.

47 M. Herklotz, J. Weiß, E. Ahrens, M. Yavuz, L. Mereacre, N. Kiziltas-Yavuz, C. Dräger, H. Ehrenberg, J. Eckert, F. Fauth, L. Giebeler and M. Knapp, A Novel High-Throughput Setup for in Situ Powder Diffraction on Coin Cell Batteries, *J. Appl. Crystallogr.*, 2016, **49**, 340–345, DOI: 10.1107/S1600576715022165.

48 O. Arcelus, J. Rodríguez-Carvajal, N. A. Katcho, M. Reynaud, A. P. Black, D. Chatzogiannakis, C. Frontera, J. Serrano-Sevillano, M. Ismail, J. Carrasco, F. Fauth, M. R. Palacin and M. Casas-Cabanas, FullProfAPP: A Graphical User Interface for the Streamlined Automation of Powder Diffraction Data Analysis, *J. Appl. Crystallogr.*, 2024, **57**, 1676–1690, DOI: 10.1107/S1600576724006885.

49 C. Marini, C. Escudero, E. Villalobos-Portillo, I. Lucentini, J. P. Albert, M. Armengol-Profitós, D. Heinis, O. Vallcorba, F. Fauth, A. P. Black, M. R. Palacin, J. B. González Fernández, Á. Baucells, J. R. G. Molinero, R. Javier Homs, N. Serra, J. Nicolàs and G. Agostini, BL16 NOTOS, an X-Ray Absorption and Diffraction Beamline for Operando Battery Studies at ALBA, *Eur. Phys. J. Plus.*, 2025, **140**(12), 1228, DOI: 10.1140/epjp/s13360-025-07170-7.

50 D. Saurel, A. Pendashteh, M. Jáuregui, M. Reynaud, M. Fehse, M. Galceran and M. Casas-Cabanas, Experimental Considerations for Operando Metal-Ion Battery Monitoring Using X-Ray Techniques, *Chem.:Methods*, 2021, **1**(6), 249–260, DOI: 10.1002/cmtd.202100009.

51 B. Ravel and M. Newville, ATHENA, ARTEMIS, HEPHAESTUS: Data Analysis for X-Ray Absorption Spectroscopy Using IFEFFIT, *J. Synchrotron Radiat.*, 2005, **12**, 537–541, DOI: 10.1107/S0909049505012719.

52 M. Fehse, A. Iadecola, M. T. Sougrati, P. Conti, M. Giorgetti and L. Stievano, Applying Chemometrics to Study Battery Materials: Towards the Comprehensive Analysis of Complex Operando Datasets, *Energy Storage Mater.*, 2019, 328–337, DOI: 10.1016/j.ensm.2019.02.002.

53 B. Puchala, J. C. Thomas, A. R. Natarajan, J. G. Goiri, S. S. Behara, J. L. Kaufman and A. Van der Ven, CASM — A Software Package for First-Principles Based Study of Multicomponent Crystalline Solids, *Comput. Mater. Sci.*, 2023, **217**, 111897, DOI: 10.1016/j.commatsci.2022.111897.

54 S. P. Ong, W. D. Richards, A. Jain, G. Hautier, M. Kocher, S. Cholia, D. Gunter, V. L. Chevrier, K. A. Persson and G. Ceder, Python Materials Genomics (Pymatgen): A Robust, Open-Source Python Library for Materials Analysis, *Comput. Mater. Sci.*, 2013, **68**, 314–319, DOI: 10.1016/j.commatsci.2012.10.028.

55 M. Leslie and N. J. Gillan, The Energy and Elastic Dipole Tensor of Defects in Ionic Crystals Calculated by the Supercell Method, *J. Phys. C: Solid State Phys.*, 1985, **18**, 973–982.

56 W. Kohn and L. J. Sham, PHYSICAL REVIEW Self-Consistent Equations Including Exchange and Correlation Effects, *Phys. Rev.*, 1965, **140**, 1133–1138.

57 I. E. Gaa, P. Hohenbergt Ecole and W. Konnt, Inhomogeneous Electron Gas, *Phys. Rev.*, 1964, **136**, 864–871.

58 G. Kresse and J. Furthmü, Efficient Iterative Schemes for Ab Initio Total-Energy Calculations Using a Plane-Wave Basis Set, *Phys. Rev. B:Condens. Matter Mater. Phys.*, 1996, **54**(16), 169–186.

59 J. Sun, A. Ruzsinszky and J. Perdew, Strongly Constrained and Appropriately Normed Semilocal Density Functional, *Phys. Rev. Lett.*, 2015, **115**(3), 036402, DOI: 10.1103/PhysRevLett.115.036402.

60 P.-F. Wang, H.-R. Yao, X.-Y. Liu, Y.-X. Yin, J.-N. Zhang, Y. Wen, X. Yu, L. Gu and Y.-G. Guo, Na+/Vacancy Disordering Promises High-Rate Na-Ion Batteries, *Sci. Adv.*, 2018, **4**, eaar6018, DOI: 10.1126/sciadv.aar6018.

61 L. F. Pfeiffer, M. Dillenz, N. Burgard, P. Beran, D. Roscher, M. Zarrabeitia, P. Drews, C. Hervoches, D. Mikhailova, A. Omar, V. Baran, N. Paul, M. Sotoudeh, M. Busch, M. Wohlfahrt-Mehrens, A. Groß, S. Passerini and P. Axmann, From Structure to Electrochemistry: The Influence of Transition Metal Ordering on Na+/Vacancy Orderings in P2-Type NaxMO2 Cathode Materials for Sodium-Ion Batteries, *J. Mater. Chem. A*, 2024, **13**, 540–560, DOI: 10.1039/d4ta04786a.

62 M. Ambrosetti, M. C. Mozzati, A. Cini, M. Fittipaldi, D. Spada, M. Sturini, I. Quinzeni and M. Bini, Physico-Chemical Features of Undoped and Fe/Cu-Doped Na0.67MnO2-Layered Cathodes for Sodium Batteries, *Appl. Sci.*, 2022, **12**(18), 12189123, DOI: 10.3390/app12189123.

63 E. McCalla, A. W. Rowe, J. Camardese and J. R. Dahn, The Role of Metal Site Vacancies in Promoting Li-Mn-Ni-O Layered Solid Solutions, *Chem. Mater.*, 2013, **25**(13), 2716–2721, DOI: 10.1021/cm401461m.

64 J. M. Paulsen and J. R. Dahn, Studies of the Layered Manganese Bronzes, Na2/3[Mn1−xMx]O2 with M=Co, Ni, Li, and Li2/3[Mn1−xMx]O2 Prepared by Ion-Exchange, *Solid State Ionics*, 1999, **126**(1–2), 3–4.

65 K. Kubota, N. Yabuuchi, H. Yoshida, M. Dahbi and S. Komaba, Layered Oxides as Positive Electrode Materials for Na-Ion Batteries, *MRS Bull.*, 2014, **39**(5), 416–422, DOI: 10.1557/mrs.2014.85.

66 Z. Lu and J. R. Dahn, In Situ X-Ray Diffraction Study of P2-Na2/3[Ni1/3Mn2/3]O2, *J. Electrochem. Soc.*, 2001, **148**(11), A1225, DOI: 10.1149/1.1407247.

67 J. Jin, Y. Liu, X. Pang, Y. Wang, X. Xing and J. Chen, A Comprehensive Understanding of the Anionic Redox Chemistry in Layered Oxide Cathodes for Sodium-Ion Batteries, *Sci. China Chem.*, 2021, **1**, 385–402, DOI: 10.1007/s11426-020-9897-8.

68 S. Daubner, M. Dillenz, L. F. Pfeiffer, C. Gauckler, M. Rosin, N. Burgard, J. Martin, P. Axmann, M. Sotoudeh, A. Groß, D. Schneider and B. Nestler, Combined Study of Phase Transitions in the P2-Type NaXNi1/3Mn2/3O2 Cathode Material: Experimental, Ab-Initio and Multiphase-Field Results, *npj Comput. Mater.*, 2024, **10**(1), 75, DOI: 10.1038/s41524-024-01258-x.

69 C. Zheng, B. Radhakrishnan, I. H. Chu, Z. Wang and S. P. Ong, Effects of Transition-Metal Mixing on Na Ordering and Kinetics in Layered P2 Oxides, *Phys. Rev. Appl.*, 2017, **7**(6), 064003, DOI: 10.1103/PhysRevApplied.7.064003.

70 M. Kubota, H. Fujioka, K. Hirota, K. Ohoyama, Y. Moritomo, H. Yoshizawa and Y. Endoh, Relation between Crystal and Magnetic Structures of the Layered Manganites La2-2xSr1+2xMn2O7 (0.30≤x≤0.50), *J. Physiol. Soc. Jpn.*, 2000, **69**, 1606–1609, DOI: 10.1143/JPSJ.69.1606.

71 H. Liu, X. Gao, J. Chen, J. Gao, S. Yin, S. Zhang, L. Yang, S. Fang, Y. Mei, X. Xiao, L. Chen, W. Deng, F. Li, G. Zou, H. Hou and X. Ji, Reversible OP4 Phase in P2–Na2/3Ni1/3Mn2/3O2 Sodium Ion Cathode, *J. Power Sources*, 2021, **508**, 230324, DOI: 10.1016/j.jpowsour.2021.230324.

72 Q. Liu, Z. Hu, M. Chen, C. Zou, H. Jin, S. Wang, Q. Gu and S. Chou, P2-Type Na2/3Ni1/3Mn2/3O2 as a Cathode Material with High-Rate and Long-Life for Sodium Ion Storage, *J. Mater. Chem. A*, 2019, **7**(15), 9215–9221, DOI: 10.1039/c8ta11927a.

73 J. W. Somerville, A. Sobkowiak, N. Tapia-Ruiz, J. Billaud, J. G. Lozano, R. A. House, L. C. Gallington, T. Ericsson, L. Häggström, M. R. Roberts, U. Maitra and P. G. Bruce, Nature of the "z"-Phase in Layered Na-Ion Battery Cathodes, *Energy Environ. Sci.*, 2019, **12**(7), 2223–2232, DOI: 10.1039/c8ee02991a.

74 L. Wang, M. Y. Sun, L. Deng, Y. Q. Zheng, X. Y. Li, Y. S. Jiang, L. Zhao and Z. B. Wang, Ti4+ Substitution Suppressing P2-O2 Phase Transition to Construct Stable P2-Na0.67Ni0.33Mn0.67O2 Cathode for Long-Term Durable Sodium-Ion Batteries, *J. Energy Storage*, 2024, **81**, 110299, DOI: 10.1016/j.est.2023.110299.

75 E. Grépin, Y. Zhou, B. Li, G. Rousse, J. M. Tarascon and S. Mariyappan, Optimal Ti-Substitution in Layered Oxide Cathodes for Na-Ion Batteries, *Chem. Mater.*, 2024, **36**, 10804–10812, DOI: 10.1021/acs.chemmater.4c02501.

76 C. Gauckler, M. Dillenz, F. Maroni, L. F. Pfeiffer, J. Biskupek, M. Sotoudeh, Q. Fu, U. Kaiser, S. Dsoke, H. Euchner, P. Axmann, M. Wohlfahrt-Mehrens, A. Groß and M. Marinaro, Detailed Structural and Electrochemical Comparison between High Potential Layered P2-NaMnNi and Doped P2-NaMnNiMg Oxides, *ACS Appl. Energy Mater.*, 2022, **5**(11), 13735–13750, DOI: 10.1021/acsaem.2c02402.

77 Y. Tang, Q. Zhang, W. Zuo, S. Zhou, G. Zeng, B. Zhang, H. Zhang, Z. Huang, L. Zheng, J. Xu, W. Yin, Y. Qiu, Y. Xiao, Q. Zhang, T. Zhao, H. G. Liao, I. Hwang, C. J. Sun, K. Amine, Q. Wang, Y. Sun, G. L. Xu, L. Gu, Y. Qiao and S. G. Sun, Sustainable Layered Cathode with Suppressed Phase Transition for Long-Life Sodium-Ion Batteries, *Nat. Sustain.*, 2024, **7**(3), 348–359, DOI: 10.1038/s41893-024-01288-9.

78 N. Tapia-Ruiz, W. M. Dose, N. Sharma, H. Chen, J. Heath, J. W. Somerville, U. Maitra, M. S. Islam and P. G. Bruce, High Voltage Structural Evolution and Enhanced Na-Ion Diffusion in P2-Na2/3Ni1/3-: XMgxMn2/3O2 ($0 \leq x \leq 0.2$) Cathodes from Diffraction, Electrochemical and Ab Initio Studies, *Energy Environ. Sci.*, 2018, **11**(6), 1470–1479, DOI: 10.1039/c7ee02995k.

79 X. Wang, L. Yin, A. Ronne, Y. Zhang, Z. Hu, S. Tan, Q. Wang, B. Song, M. Li, X. Rong, S. Lapidus, S. Yang, E. Hu and J. Liu, Stabilizing Lattice Oxygen Redox in Layered Sodium Transition Metal Oxide through Spin Singlet State, *Nat. Commun.*, 2023, **14**(1), 7665, DOI: 10.1038/s41467-023-43031-6.